DESIGN, TEST, AND CALIBRATION OF THE UTAH STATE UNIVERSITY FLOATING POTENTIAL PROBE

by

Jessica D. Gregory

A thesis submitted in partial fulfillment
of the requirements for the degree

of

MASTER OF SCIENCE

in

Electrical Engineering

Approved:

Dr. Charles M. Swenson Major Professor	Dr. Todd K. Moon Committee Member
Dr. Chris Winstead Committee Member	Dr. Byron R. Burnham Dean of Graduate Studies

UTAH STATE UNIVERSITY
Logan, Utah

2010

Abstract

Design, Test, and Calibration of the Utah State University Floating Potential Probe

by

Jessica D. Gregory, Master of Science

Utah State University, 2010

Major Professor: Dr. Charles M. Swenson
Department: Electrical and Computer Engineering

The ionosphere is a conducting layer in the Earth's upper atmosphere and is the nearest naturally occurring plasma environment. Inherent to all plasma environments is an electric field. Currently, the double electric field probe is the most successful instrument for measuring the electric fields of space plasmas. Utah State University/Space Dynamics Lab has developed a double electric field probe, called the Floating Potential Probe (FPP), with a slightly different instrumentation approach than what has been done previously. The FPP is one component of a suite of instruments that launched in fall of 2007 from Wallops Island, Virginia, as part of NASA's sounding rocket program to an approximate altitude of 450km. This mission is nicknamed "The Storms Mission."

In general, an electric field probe acts as a voltmeter to measure the electric potential between a probe located near the end of a long boom and the skin of the rocket. This measurement is also called the floating potential. To obtain electric field measurements, the floating potential is gathered from two probes located 180^o apart and differenced to calculate the electric potential between probes and thereby the ambient electric field. Historically, this has been accomplished with an entirely analog circuit implementation. For the Storm Mission, the signals are digitized before the differencing occurs. Then during data analysis, the signals can either be differenced digitally to produce the ambient electric field or summed

to observe the floating potential of the payload skin. Additionally, the signals are digitized to 20 bits giving a far greater dynamic range than is typically achieved in similar direct current (DC) coupled instruments. This thesis discusses the theory, design, test, and calibration efforts of the FPP for the Storms Mission.

(**??** pages)

Acknowledgments

My gratitude extends to all those who have encouraged and supported me throughout this effort. Specifically, I want to thank Dr. Charles Swenson for giving me the opportunity to be a member of the Storms Mission team, for his invaluable guidance, and for his patience. My appreciation goes out to the Storms Mission team, namely, Albert Hummel, Wayne Sanderson, Timothy Campbell, Jason Bingham, and Michael Holt, for all their hard work and effort to make the Storms Mission a success. I have been blessed by an incredible family, especially my parents, Michael and Vicki, and am grateful for their unconditional love, support, strength, and encouragement. I am thankful for all of my amazing friends who have been there for me when I needed it most. Lastly, I would be remiss if I didn't thank my Father Above for every challenge and blessing.

Jessica D. Gregory

Contents

List of Tables

List of Figures

Acronyms

ADC	Analog/Digital Converter
DCP	Direct Current Probe
EFI	Electric Field Instrument
EUV	Extreme Ultraviolet
FPGA	Field Programmable Gate Array
FPP	Floating Potential Probe
GPS	Global Positioning System
HATI	Hanson Anemometer for Thermospheric Investigations
LCTE	Low-Cost Telemetry Encoder
NASA	National Aeronautics and Space Administration
PCB	Printed Circuit Board
PFP	Plasma Frequency Probe
PIP	Plasma Impedance Probe
SDL/USU	Space Dynamics Laboratory/Utah State University
SIP	Sweeping Impedance Probe
SLP	Sweeping Langmuir Probe
USU	Utah State University
UTD	University of Texas - Dallas
UV	Ultraviolet

Chapter 1

Introduction

1.1 General Introduction

The ionosphere is a complex and dynamic region of the atmosphere that extends from 60 to 1000km above the surface of the Earth. It is a transition region from the relatively un-ionized lower atmosphere to the fully ionized plasmasphere. Ionization occurs as high energy photons from the sun (at ultraviolet(UV), extreme ultraviolet(EUV), and x-ray wavelengths) bombard molecules of oxygen and nitrogen causing an electron to be dislodged from the neutral molecule. The collection of free electrons and ionized molecules is called plasma.

The ionosphere can be separated into layers that are distinguished by their composition and altitude. The D-layer ranges from 60 to 100km and mostly consists of nitric oxide(NO). The E-layer ranges from 100 to 150km and mostly consists of molecular oxygen(O_2). The F-layer ranges from 150 to 1000km and mostly consists of atomic oxygen(O). These layers can fluctuate in altitude, ion composition, and density depending on the time of day, time of season, latitude, amount of radiation from the sun, and strength of Earth's magnetic field (see fig. **??** [**?**]) [**?**].

The ionosphere plays an important role in terrestrial and space communications. At frequencies below critical frequency, radio waves bounce off the ionosphere and allow for long range communications. In this way the ionosphere is used by international broadcasters, commercial shipping businesses, military communication and surveillance operations, and amateur radio enthusiasts. Above the critical frequency, radio waves pass through the ionosphere allowing for communication with spacecraft. However, solar flares and coronal

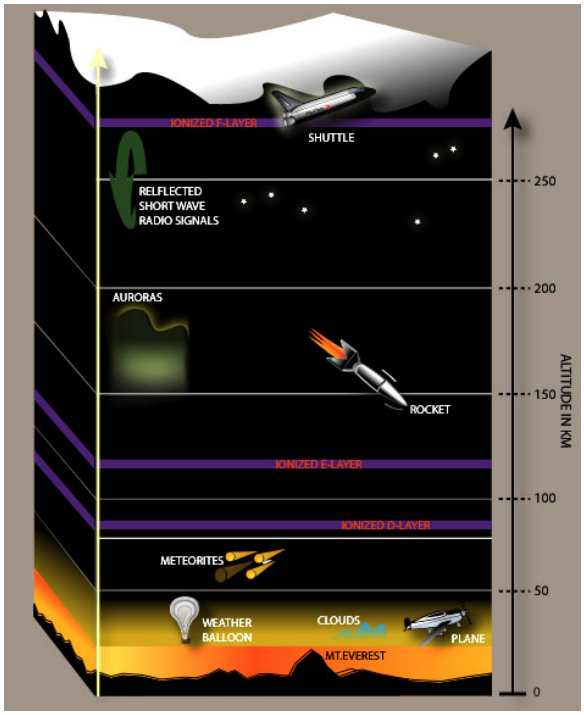

Fig. 1.1: The structure of the ionosphere.

mass ejections can create higher or lower density structures within the ionosphere and disrupt all forms of communication.

Enough is understood about the ionosphere to take advantage of its properties for communication purposes, but there is still a great deal to learn about its physics, chemical composition, and response to solar influence. The dilemma comes in reaching this part of the atmosphere for direct observations. Aircraft and high-altitude balloons generally cannot fly above 50km while satellites cannot orbit below 250km without reentering the atmosphere relatively quickly. This leaves the options of either making remote observations from below with ground stations, from above with satellites, or making *in-situ* observations using rockets as they pass through the region. Although their flight time is short, rockets have the advantage that their launch can be timed to specific events. One such rocket mission, nicknamed "The Storms Mission," is being conducted to better understand ionospheric anomalies and irregularities in the ionosphere that are driven by large terrestrial weather events in the troposphere.

1.2 Storms Mission

The Space Dynamics Laboratory/Utah State University (SDL/USU) and the University of Texas Dallas (UTD) collaborated on a NASA sounding rocket mission titled "Investigation of Mid-Latitude Ionospheric Irregularities Associated with Terrestrial Weather Systems" or "The Storms Mission" for short. The rocket, designated by NASA as 36.218, was scheduled to launch during the fall of 2007 from Wallops Island, Virginia, to an approximate altitude of 450km. It was planned to launch the rocket over a large cell of thunderstorms or, under ideal conditions, over a hurricane or tropical storm. The instruments on the main payload (see fig. **??**) will be supplied by UTD and include a Hanson Anemometer for Thermospheric Investigations (HATI) to measure the direction and strength of the ionospheric neutral winds and a Electric-Field Instrument (EFI) to measure the quasi-DC electric fields in the ionosphere. SDL/USU will provide the instruments on the daughter payload that will measure electron temperature, electron density, electron neutral collision frequency, spacecraft floating potential, and electric field. To accomplish this, the subpayload will consist of a Plasma Frequency Probe (PFP), a Sweeping Impedance Probe (SIP), a DC Langmuir Probe (DCP), a Sweeping Langmuir Probe (SLP), and a Floating Potential Probe (FPP). This paper will cover the design and implementation of the FPP.

In addition to the data collected from the instruments on the rocket, a number of ground-based sensing stations will aid in the investigations. The Weather Station at Wallops Island will monitor the location, direction, and speed of weather systems. The Dynasonde at Wallops Island will use radio wave reflections to monitor the disturbed or undisturbed state of the ionosphere. The Scintillation Receivers will collect electron density profiles which will be compared to *in-situ* data. The TIDDBIT HF radar will be used to monitor undulations on the bottomside of the ionosphere. Finally, the Array of Ground Based Receivers will collect data from about 100 line-of-sight GPS signals that propagate through the ionosphere over Wallops Island.

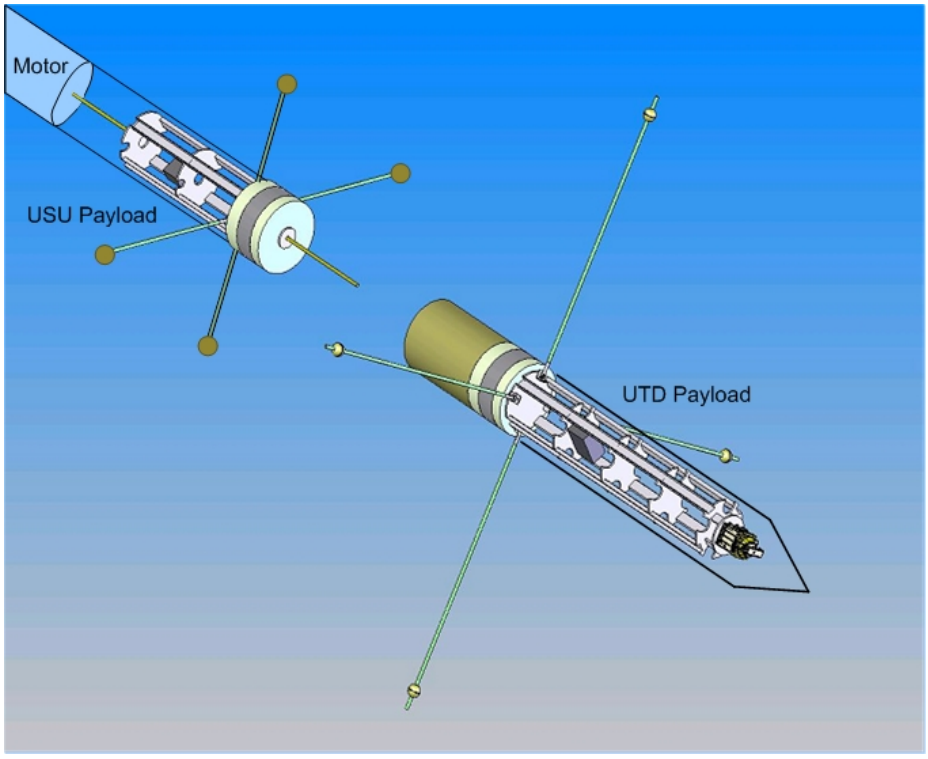

Fig. 1.2: The Tropical Storm Rocket payloads.

1.2.1 Science

The goal of the Storms Mission is to make further investigations into understanding and answering the following two questions: 1) What is the cause of the spread in altitude signatures of ionosonde (or dynasonde) observations of the reflection height of low-frequency radio waves? 2) What effect does a large tropospheric weather system have on the density structures of the ionosphere above it?

A ground-based ionosonde instrument operates by broadcasting a range of radio waves into the atmosphere and observing the length of time required for the radio waves to bounce off the ionosphere and reflect back to Earth. From these measurements, the ionosonde is able to capture the altitude of the reflection point for the various frequencies. The ionosonde at Wallops Island, VA sweeps through a range of frequencies from about 1MHz to 8MHz. The beam of the ionosonde is very large and encompasses nearly the entire observable sky. Figure **??** presents data taken three days apart by the ionosonde at Wallops. The panel on the left shows the radio wave reflections under normal atmospheric conditions. The panel

on the right shows a significant spread in the altitude of the reflection points. The spread signature could either result from the variations in height as the ionosonde looks at the entire sky or from some type of localized density disturbance within the radio beam.

A connected scientific experiment to these science questions occurred in September 1995 when a USU-built instrument was launched over a cell of thunderstorms [**?**]. The electron density altitude profile (fig. **??**) showed significant atypical structuring with altitude in the 240km to 260km altitude range. It has been suggested that atmospheric buoyancy waves (commonly referred to as gravity waves) were being generated by the storm and propagating upwards thus disturbing the ionosphere. The presence of gravity waves cause the observed small-scale structuring seen in fig. **??**. The question remains as to whether these structures are caused by the wind shears created by gravity waves, the turbulent breakup of the gravity wave, or a plasma instability seeded by the presence of the gravity waves.

1.2.2 Payload

The Storms Mission consists of two instrumented payloads. The instruments on the main payload are being developed by UTD and consist of the HATI, to measure neutral winds, and the EFI, to measure quasi-DC electric fields. In order for the HATI instrument to collect good data, the payload must always be aligned with the velocity vector. A cold gas attitude control system will maintain occasional thruster firings to keep the payload pointing in the correct direction. However, these thruster firings could interfere with the instruments being developed by USU and therefore a separate sub-payload for these instruments was required. A conceptual drawing of the USU sub-payload for the Storms Mission is presented in fig. **??**.

The five instruments on the sub-payload are implemented on two electronics boards. One board contains the PFP, SIP, and DCP instruments whose sensors are located on the probe that is pointed in the fore direction of the rocket. The design and testing of these three instruments are the subject of another thesis [**?**]. The second electronics board contains the SLP and the FPP. The SLP sensor is located in the aft direction of the rocket and the FPP sensors are the four probes that are located perpendicular to the rocket spin axis and

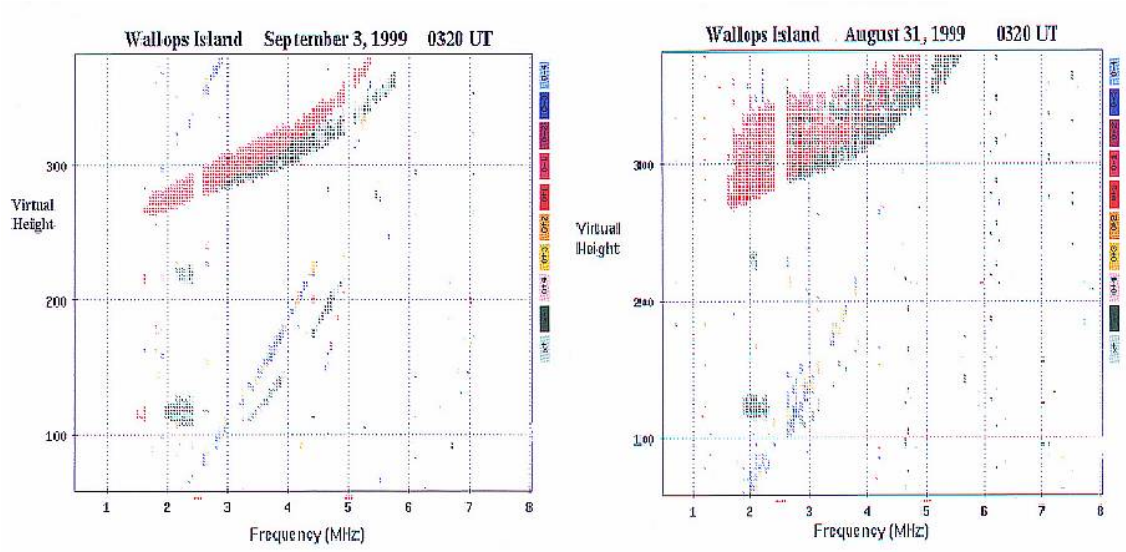

Fig. 1.3: Ionosonde data illustrating the virtual hight of the ionosphere. Data taken from Wallops Island, Virginia, on September 3, 1999 and August 31, 1999. (Courtesy of Terry Bullet AFRL.)

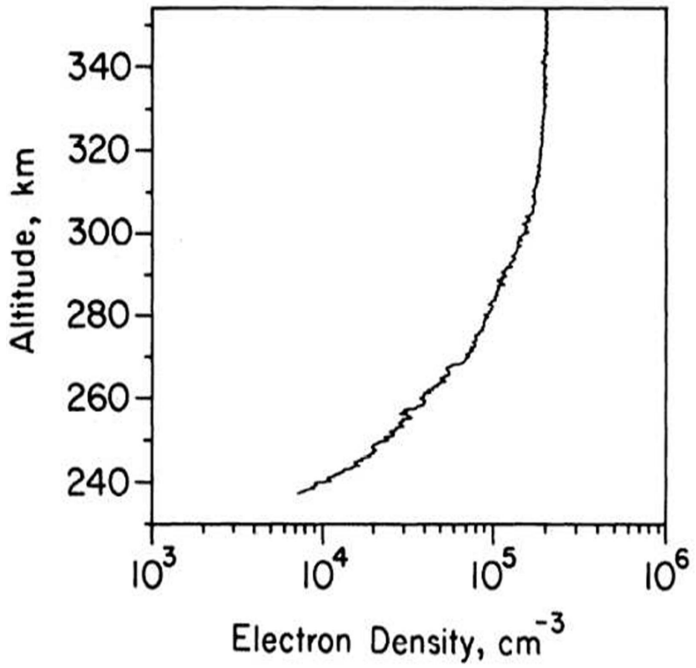

Fig. 1.4: Upleg plasma density profile from a Plasma Frequency Probe on a sounding rocket launched from Wallops Island, Virginia, in September 1995.

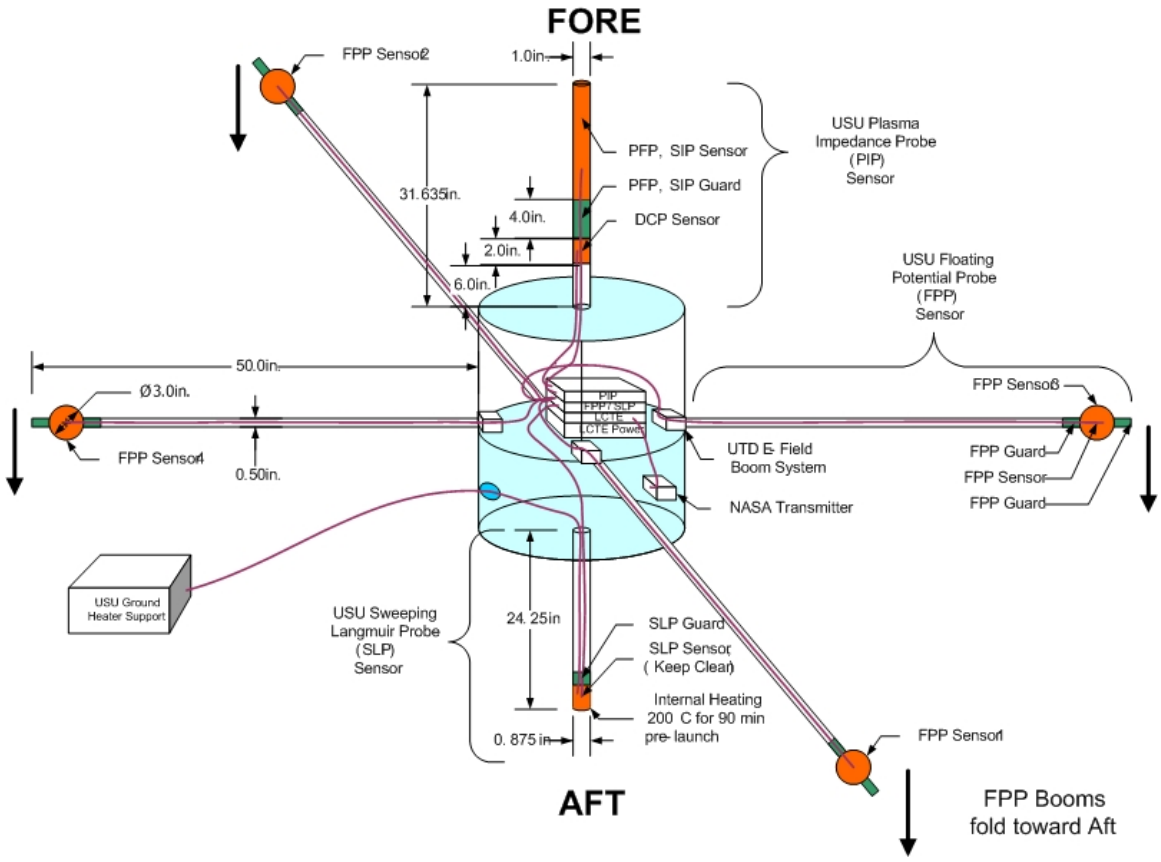

Fig. 1.5: The SDL/USU Tropical Storm payload.

separated from each other by 90^o. Both electronics boards are connected to a Low-cost Telemetry Encoder (LCTE) that has also been designed and built by USU [**?**, **?**].

1.2.3 Telemetry Requirements

Ideally, the sampling rate of each instrument is determined by the spatial resolution that is reasonably required for the science objectives. However, because it is assumed that the structures associated with the science questions are stationary in the ionosphere relative to the speed of the rocket passing through them it does not make sense to make spatial samples at a scale smaller than the dimensions of the sensor. For the Storms Mission, the spatial resolution ranges between 0.1 to 100m depending on the instrument. The velocity of the rocket is expected to be 1km/s in the regions of interest but could vary between 0.5km/s and 3km/s. Table **??** shows the designed sample rates and spatial resolutions at 0.5km/s and 3km/s for each instrument.

1.3 Instrumentation Techniques

All of the instrumentation techniques that are part of the Storms Mission have a long and successful heritage. For decades at USU instruments have been designed, redesigned, and flown on a variety of spacecraft using these measurement methods. A brief overview of each instrumentation technique is presented.

Table 1.1: Required data rates for each science channel.

Plasma Characteristic	Sample Rate	Spatial Resolution at 0.5km/s	Spatial Resolution at 3km/s
PFP - absolute electron density	2441 Hz	0.20	1.23 m
SIP - absolute electron density	76.29 Hz	6.55	39.3 m
DCP - electron density variations	2441 Hz	0.20	1.23 m
SLP - electron temperature	38.15 Hz	13.11	78.6 m
FPP - spacecraft floating potential	4883 Hz	0.10	0.61 m

1.3.1 Plasma Frequency Probe

The first PFP was flown over 30 years ago has since progressed through multiple redesigns and sounding rocket launches until it is now accepted as a reliable, accurate method for measuring electron density and temperature throughout the E and F regions of the ionosphere. The PFP provides excellent time and frequency resolution for determining small-scale plasma instabilities and is insensitive to changes in spacecraft potential and probe surface contamination both of which can introduce significant measurement errors in Langmuir probes [**?**]. It operates by utilizing a control loop which tracks the upper hybrid frequency where there is a sharp transition in the antenna current and voltage [**?**]. Recent USU sounding rocket campaigns that have flown the PFP include: Thunderstorm II (38.007), Auroral Turbulence (40.005), Thunderstorm III (36.111), SAL (21.117), CODA I (21.121), CODA II (21.128), E-Winds (41.036, 41.037, 27.144, 41.038), and Kwajalein-Hysell (29.036, 29.037). The design and implementation of the PFP as well as the SIP and the DCP are the topic of another thesis [**?**].

1.3.2 Sweeping Impedance Probe

The SIP shares a similar history with the PFP. However, instead of tracking the upper hybrid frequency, the SIP sweeps over a predetermined set of radio frequencies and measures the corresponding impedance of the probe. In this way, the plasma density can be determined from the location of the upper hybrid resonance and other parameters from the shape of the impedance curve.

1.3.3 DC Langmuir Probe

The DCP and SLP measurement techniques were pioneered in the 1920s by Irving Langmuir, one of the first scientist to study plasmas. The DCP operates by applying a voltage, biased to a fixed potential relative to the rocket surface, to an electrode immersed in a plasma. The instrument then measures the current flowing to or from the electrode. The DCP for the Storms Mission is biased at -7 volts, thus operating in the ion saturation region of the Langmuir curve and provides a relative ion density measurement.

1.3.4 Sweeping Langmuir Probe

The SLP operates in the same way as the DCP but, instead of the biased voltage being held constant, it sweeps from -1 to 5 volts in 12mV steps. For the Storms Mission the SLP will be held at a constant biased voltage of +3V for most of the time and will only sweep once every 20 seconds. This compromise was made because the small surface area of the daughter payload makes it possible for the SLP to change the payload surface potential and potentially corrupt the FPP measurements. In this way, the FPP measurements remain true and the SLP is still able to make reliable electron density measurements and occasional temperature measurements.

1.3.5 Floating Potential Probe

The double probe technique using analog instrumentation amplifiers has been the most successful instrument for measuring electric fields in space [**?**]. In general, the FPP acts as a voltmeter to measure the electric potential between each probe and the skin of the rocket or, in other words, the floating potential of the sensor. This data is then differenced to calculate the electric potential between probes and thereby the ambient electric field. The FPP built for the Storms Mission uses a slightly different instrumentation approach to measure the electric field than what has been done previously. Instead of an entirely analog circuit implementation, the signals are digitized before the differencing occurs. Then during data analysis, the signal can be differenced digitally to produce the ambient electric field or summed to obtain the floating potential of the payload skin. Additionally, the signals are digitized to 20 bits giving a far greater dynamic range than is typically achieved in similar DC coupled instruments.

1.4 Thesis Overview

This thesis examines if a high precision set of floating potential probes can be designed, implemented, and calibrated to meet the science requirements for the Storms Mission. The approach to this instrumentation for measuring electric fields and vehicle floating potential is unique. The signal are measured differentially and digitized earlier in the instrument chain.

In Chapter 2 we present a system overview of the FPP detailing electrical, mechanical, telemetry, and calibration designs of the FPP. Chapter 3 provides an in-depth look at the FPP's electrical design, specifically, the analog front end, the A/D control, and the digital control. Chapter 4 demonstrates the current functionality of the FPP and calibration. Chapter 5 concludes this thesis and contains recommendations as to how the FPP could be improved.

Chapter 2

Theory of the Floating Potential Probe

The electrical properties of a conducting sensor or probe immersed in plasma are known to the extent that they can be used to measure the plasma properties. With the proper configuration and sensitivity of the measuring electronics these types of probes can be used to measure the density, temperature, composition, and bulk drift of the plasma. In this chapter we review the basic theory of electrical probes in plasma and then relate this theory to the engineering requirements of the Utah State University Floating Potential Probe (USU-FPP or FPP for short). This instrument is designed to measure electric fields around and the floating potential of the Storms payload.

2.1 Probe Collection Currents

The key to understanding the operation of the USU-FPP is to understand the response of a passive, electrically-isolated conductor immersed in plasma. A charge is transferred to the conductor every time an electron or ion encounters the surface. Initially, the resulting current due to electrons is larger than the current due to ions because of the higher random velocity of the lighter electrons. This larger electron current quickly causes the conductor to charge and develop a negative potential with respect to the background plasma. An equilibrium is reached by slightly attracting the ions while turning away a significant number of low energy electrons. A positive ion sheath is thus formed around the conductor that is a few Debye lengths, λ_d, thick. In MKS units the Debye length is given by

$$\lambda_d = \sqrt{\frac{\epsilon_o k_b T_e}{n e^2}}, \tag{2.1}$$

where ϵ_o is the permittivity of free space, k_b is Boltzmann's constant, T_e is electron temperature, n is electron density, and e is the electron charge. Outside of this sheath region

the charges present on the conductor cannot be detected and the surrounding plasma is undisturbed.

The equations describing the electron and ion currents to a probe at a potential relative to the plasma can be developed under the assumption that the probe dimensions are much larger than the Debye length of the plasma. This is the so called "thin sheath" approximation in which the sheath dimensions do not add to the effective surface area of the probe. We assume that the probe is held at a potential, ϕ_o, relative to some arbitrary reference point. For a probe on a spacecraft this reference point would be the electrical ground of the measurement electronics which is typically tied to the spacecraft structure. The potential of the undisturbed plasma, ϕ_p, is also referenced to this same point. The reference direction for the currents is chosen to be positive into the probe.

We first consider the case where $\phi_o \geq \phi_p$. The potential on the conductor is attracting electrons from the surrounding plasma but only the electrons within the sheath are affected. The number of electrons attracted must be balanced by the number of new electrons entering the sheath region and only the electrons with thermal motion towards the probe will become sheath electrons. This electron current is independent of applied attracting potential and therefore called the saturation current which is given by

$$I_e = -Aen\sqrt{\frac{k_b T_e}{2\pi m_e}}, \tag{2.2}$$

where A is the surface area of the probe, e is the electron charge, and m_e is the mass of the electrons and the other constants are previously defined. For the case where $\phi_o < \phi_p$, the electrons with kinetic energy less than $e\phi_o$ cannot reach the surface of the probe being turned away by the negative potential. If the electrons have a Maxwellian velocity distribution then the electron current behaves exponentially with potential according to

$$I_e = -Aen_e\sqrt{\frac{k_b T_e}{2\pi m_e}}\exp\left(\frac{e(\phi_o - \phi_p)}{k_b T_e}\right). \tag{2.3}$$

This is known as the electron retardation current and is shown with the electron saturation current in fig. **??**. The equations for the thermal ion currents are similarly developed and with the assumption that the conductor is stationary or moving much slower than the ion thermal velocity. By knowing that the density of electrons is equal to the density of ions in the ionosphere and by replacing T_e with T_i and m_e with m_i in the previous equations we have

$$I_i = Aen\sqrt{\frac{k_b T_i}{2\pi m_i}}, \tag{2.4}$$

which is an expression for the ion saturation current when $\phi_o < \phi_p$. Similarly we get

$$I_i = Aen\sqrt{\frac{k_b T_i}{2\pi m_i}} \exp\left(\frac{-e(\phi_o - \phi_p)}{k_b T_i}\right), \tag{2.5}$$

for the ion retardation current when $\phi_o \geq \phi_p$. Figure **??** shows the ion currents. Note that the electron saturation current is $\sqrt{m_i/m_e}$ or about 50 times greater than the ion saturation current.

2.2 Probe Floating Potential

The floating potential, ϕ_f, of a conducting body is the steady state voltage reached such that all of the currents to the surface of the body are balanced. These currents are illustrated in fig. **??**. In addition to the electron, I_e, and ion, I_i, currents from the background thermal plasma we have included currents due to measuring electronics, I_m, and other sources such as photoelectrons or radiation particle effects, I_{other}. The equilibrium condition requires

$$I_e + I_i = I_m + I_{\text{other}}. \tag{2.6}$$

The currents due to the surrounding plasma dominate all other currents for a probe in the Earth's dense ionosphere. This is would not be the case for probes in the solar wind or at geosynchronous orbit where photoelectron emission currents are equally important. The floating potential of the conductor is thus effectively determined by considering when the magnitude of the electron current approximately equals the magnitude of the ion current

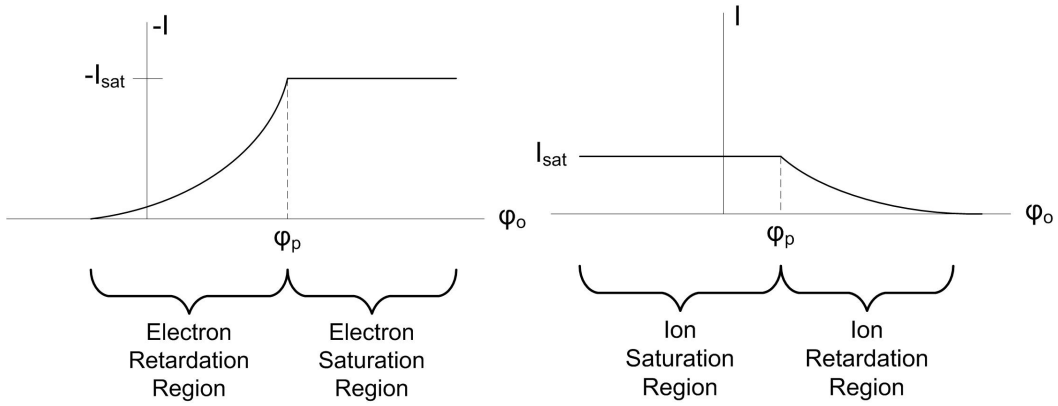

Fig. 2.1: Electron current (left) and Ion current (right) as a function of applied potential, ϕ_o for conditions of a thin plasma sheath.

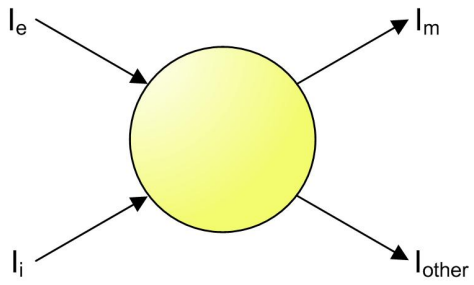

Fig. 2.2: Currents applied to a conductor in a plasma.

assuming that I_m and I_{other} are small relative to I_i. This is shown in fig. **??**. These magnitudes are approximately equal when the electron current is in the retardation region and the ion current is in the saturation region as shown. Equation (**??**) then becomes

$$-Aen\sqrt{\frac{k_bT_e}{2\pi m_e}}\exp\left(\frac{e(\phi_o-\phi_p)}{k_bT_e}\right)+Aen\sqrt{\frac{k_bT_i}{2\pi m_i}}=I_m+I_{\text{other}}. \tag{2.7}$$

Under the assumption that the temperature of the plasma is relatively uniform ($T = T_e = T_i$), eq. (**??**) can be solved for the specific potential the conductor reaches at equilibrium

$$\phi_f=\phi_p+\frac{k_bT}{e}\ln\left(\sqrt{\frac{m_e}{m_i}}-\frac{I_m+I_{other}}{An_oe\sqrt{\frac{k_bT}{2\pi m_e}}}\right). \tag{2.8}$$

Ideally, the measurement current, I_m, and the other currents, I_{other}, can be kept small so they can be ignored. Under this assumption, eq. (**??**) further reduces to

$$\phi_f=\phi_p+\frac{k_bT}{e}\ln\left(\sqrt{\frac{m_e}{m_i}}\right). \tag{2.9}$$

For ionospheric plasma with temperatures ranging between 300K and 2000K, the floating potential is about 0.10 to 0.65 Volts from the plasma potential.

2.3 Floating Probe Sheath Circuit Model

The nonlinear expression for the behavior of a probe as a function of measurement current, eq. (**??**), is not necessarily intuitive. The potential that a conductor floats to in

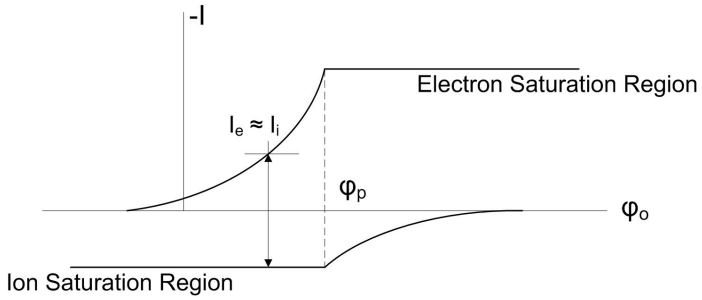

Fig. 2.3: Electron and Ion currents as a function of potential on a flat place conductor.

a plasma is dependent upon the measurement current, I_m, of any instrumentation used to observe its potential. A linear model for this effect can be derived from eq. (**??**) under the assumption that $I_{other} = 0$. A Taylor Series expansion in I_m about the point $I_m = I_b$ where I_b is the input bias current of the instrumentation is given by

$$\phi_f = \phi_f(I_b) + \left.\frac{d\phi_f}{dI_m}\right|_{I_m=I_b} I_m + \frac{1}{2}\left.\frac{d^2\phi_f}{dI_m^2}\right|_{I_m=I_b} I_m^2 + \ldots \,. \tag{2.10}$$

For small measurement currents the second and higher order terms in I_m can be neglected relative to the first two terms. The zeroth order term is the floating potential, ϕ_f, of the sensor. The sheath potential, ϕ_s, is given by the difference between the floating potential and plasma potential, $\phi_s = \phi_f - \phi_p$. This is the potential seen by charged particles traversing between the distant plasma and the surface of the probe and is given by

$$\phi_s = \frac{K_b T}{e} \ln\left[\sqrt{\frac{m_e}{m_i}} - \frac{I_b}{An_o e\sqrt{\frac{K_b T}{2\pi m_e}}}\right]. \tag{2.11}$$

The first order term in eq. (**??**) is the dynamic resistance of the plasma sheath around the probe at the floating potential of the probe and is given by

$$R_s(I_b) = \left.\frac{d\phi_f}{dI_m}\right|_{I_m=I_b} = \frac{K_b T}{e}\left[An_o e\sqrt{\frac{k_b T}{2\pi m_i}} - I_b\right]^{-1}. \tag{2.12}$$

Thus a circuit model for a probe in plasma consists of a voltage source given by eq. (**??**) in series with a resistance given by eq. (**??**). We note that the sheath resistance is a function of the collecting area but is typically on the order of $10^6 - 10^7\Omega$.

2.4 Electric Field Double Probe

The previous sections have presented the physics of a single isolated probe in a plasma. The well-known electric field double probe is constructed from two such identical probes immersed in a plasma but separated by a distance, d [**?**, **?**, **?**]. This distance can be represented as a vector pointing from sensor 1 to sensor 2 using the notation $\vec{d}_{1,2}$. Ideally the

potential difference between these probes is given by

$$\phi_{1,2} = \vec{E} \cdot \vec{d}_{1,2}, \tag{2.13}$$

where $\vec{E}$ is the ambient electric field to be observed. The measured voltage divided by the separation distance, d, gives the component of the electric field projected in the direction of the vector $\vec{d}_{1,2}$. Multiple double probes aligned along different axes can be used to determine the entire vector electric field.

A double probe instrument including sheath effects, surface work functions, and electronics can be modeled by the circuit diagram shown in fig. **??**. The assumed ambient electric field to be observed is modeled as the voltage source at the bottom of the diagram. The sheath voltage for each probe is also modeled as a voltage source, ϕ_s, with small perturbations in the measurement current modeled as the resistance, R_s. The work function of the probes for the emission and collection of electrons must also be accounted for. This is done by the voltage source ϕ_W. Lastly, the analog circuitry of the measurement instrument is simply modeled with an input resistance, R_m. By denoting the current around this loop as i_m and applying Kirchoff's Voltage law, an expression for the measurement current becomes

$$E \cdot \vec{d_{1,2}} = -\phi_{s1} + i_m R_{s1} + \phi_{W1} + i_m R_m - \phi_{W2} + i_m R_{s2} + \phi_{s2}. \tag{2.14}$$

If eq. (**??**) is solved for i_m and then multiplied by R_m the following expression for the measured voltage, ϕ_m is found as

$$\phi_m = i_m R_m = \frac{\vec{E} \cdot \vec{d} + (\phi_{s1} - \phi_{s2}) + (\phi_{W2} - \phi_{W1})}{1 + R_{s1}/R_m + R_{s2}/R_m}. \tag{2.15}$$

Equation (**??**) demonstrates that for a double probe to operate close to ideal as described in eq. (**??**) a few criteria need to be met. First R_m must be greater than either R_{s1} or R_{s2} by at least an order of magnitude so that the denominator approaches unity. Additionally, the floating potentials and the work functions for the two probe surfaces must be matched. This is difficult to achieve and in practice results in a small DC offset in the

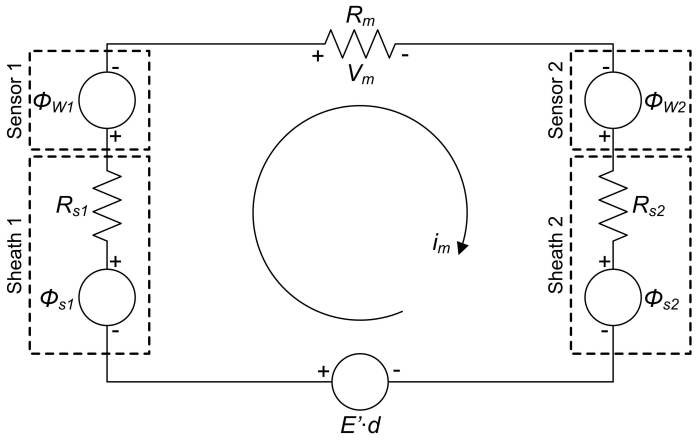

Fig. 2.4: A double probe circuit model with an applied external electric field.

measurement. The $\vec{E} \cdot \vec{d}$ term becomes a sinusoidal signal for a double probe spinning in space about an axis perpendicular to $\vec{d}$. Offsets can be identified under these conditions and removed as long as they are slowly varying relative to the spin rate.

The FPP is a double probe as just described but electrically implemented uniquely. The typical electric field double probe uses high input resistance analog instrumentation amplifiers to measure the voltage difference between two identical probes. This signal is then digitized and transmitted to the ground for analysis. The FPP measures the difference between a probe and the payload skin as is illustrated in fig. **??**. The FPP consists of four such probes deployed every 90° in a plane. Each of these measurements is digitized simultaneously and transmitted for analysis. By differencing opposite channels during analysis a signal identical to the typical double probe is developed. Essentially the FPP just moves the digitization of the signals to an earlier point in the signal chain than has been typical.

The effects of differencing the signals either within the instrument or during data analysis can be analyzed using the models previously developed. The equation describing the signal from probe 1 is of the same form as eq. (**??**) but with probe 2 being replaced by the large area of the spacecraft skin denoted with the subscript 0 as

$$\phi_{1,0} = \frac{\vec{E} \cdot \vec{d}_{1,0} + (\phi_{s1} - \phi_{s0}) + (\phi_{W0} - \phi_{W1})}{1 + R_{s1}/R_{m1} + R_{s0}/R_{m1}}, \tag{2.16}$$

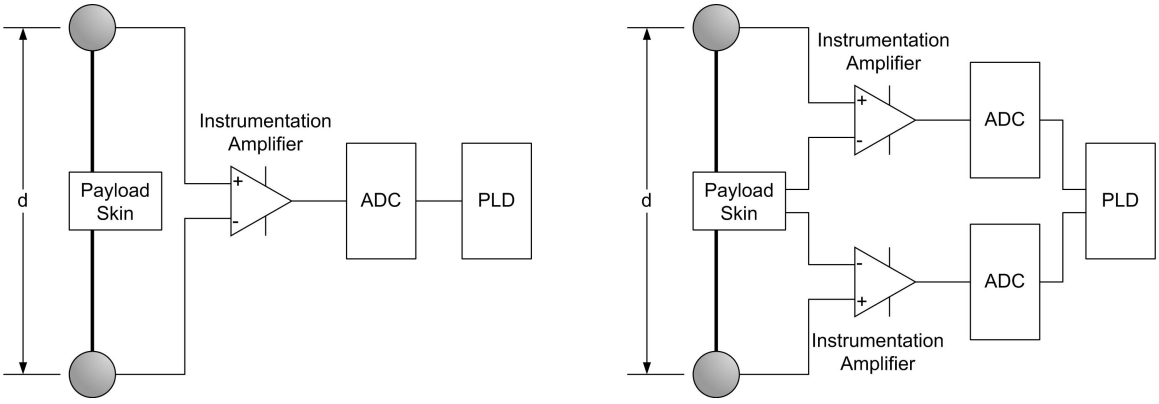

Fig. 2.5: The diagram on the left shows the conventional configuration of an Electric Field Probe. The diagram on the right shows how USU's FPP is configured to collect both floating potential and electric field measurements.

where $\vec{d}_{1,0}$ is a vector from sensor 1 to the spacecraft of length $d/2$. Similarly, the equation for probe 2 is given by

$$\phi_{2,0} = \frac{\vec{E} \cdot \vec{d}_{2,0} + (\phi_{s2} - \phi_{s0}) + (\phi_{W0} - \phi_{W2})}{1 + R_{s2}/R_{m2} + R_{s0}/R_{m2}}, \tag{2.17}$$

where $\vec{d}_{2,0}$ is a vector from sensor 2 to the spacecraft of length $d/2$ and directed opposite to $\vec{d}_{1,0}$. These two measurements are then differenced to give the measurement $\phi_{1,2}$ which is the electric field projected along the direction from sensor 1 to sensor 2. If the input resistances are sufficiently large compared to sheath resistances, this gives

$$\phi_{1,0} - \phi_{2,0} \approx (\vec{E} \cdot \vec{d}_{1,0} - \vec{E} \cdot \vec{d}_{2,0}) + (\phi_{s1} - \phi_{s0}) + (\phi_{W0} - \phi_{W1}) - (\phi_{s2} - \phi_{s0}) - (\phi_{W0} - \phi_{W2}), \tag{2.18}$$

which simplifies to

$$\phi_{1,2} = (\vec{E}_{1,2} \cdot \vec{d}) + (\phi_{s1} - \phi_{s2}) + (\phi_{W2} - \phi_{W1}). \tag{2.19}$$

Ideally the work functions and sheath potentials are identical for the two probes thus producing eq. (**??**).

Fundamentally, the FPP approach has identical problems to the more traditional instrumentation amplifier approach. Internally, any instrumentation amplifier determines the

voltage on each input with respect to ground before differencing them. Gain or other mismatches in the internal channels contribute to the common mode rejection ratio for the device. Similarly, careful calibration is required for each channel of the FPP to reduce the common mode problems. The advantage of the approach occurs where there are more than two probes deployed on the spacecraft. Electric field measurements can be computed from every combination of sensors during data analysis.

2.5 Floating Potential Probe

In some cases it is desirable to observe the floating potential of the spacecraft as it impacts the performance of other instrumentation. A Langmuir probe is included on the the Storms payload that is expected to significantly disturb the floating potential of the payload. This was the primary motivation for developing the FPP. Information on the payload floating potential can be obtained by summing data from opposing measurements. The sum of eq. (**??**) and (**??**), along with the assumption that input resistances are large, gives

$$\phi_{1,0}+\phi_{2,0} \approx (\vec{E}\cdot\vec{d}_{1,0}+\vec{E}\cdot\vec{d}_{2,0})+(\phi_{s1}-\phi_{s0})+(\phi_{W0}-\phi_{W1})+(\phi_{s2}-\phi_{s0})+(\phi_{W0}-\phi_{W2}), \quad (2.20)$$

which simplifies to

$$\phi_{1+2} = -2\phi_{s0} + \phi_{s1} + \phi_{s2} + 2\phi_{W0} - \phi_{W1} - \phi_{W2}. \quad (2.21)$$

It is expected that the work function will not change significantly over time and that the potential of the spheres will only change slowly over time. Therefore, any sudden or fast changes with time are due to changes in the floating potential of the payload which is observed by eq. (**??**).

2.6 Summary of Requirements

There are a number of requirements and constraints that the FPP instrumentation and approach must meet so that both the electric field and the changing floating potential of the payload can be observed. They are as follows:

1. The input resistances R_{m1} and R_{m2} must be large compared to the sheath resistance of the probes and payload skin, R_{s0}, R_{s1}, and R_{s2}.

2. The input bias current of the instrument must be small so as not to perturb the floating potential of the sensor.

3. The difference between the sheath potentials must be as small as possible ($\phi_{s1} - \phi_{s2} = 0$). This is achieved by making the probe material, geometry, and orientation be nearly identical.

4. The work functions of the two probes must also be nearly identical ($\phi_{W2} - \phi_{W1} = 0$). The work function is dependent both on the material of the conductors and the cleanliness of the surfaces.

Chapter 3

Design of the USU-FPP

Simply stated, the USU-FPP is a very high precision volt meter that measures the potential difference between two conducting surfaces. What is called the FPP on the Storms payload is actually four instruments each taking its own floating potential measurement and then sampled synchronously with the others. The sensors for the FPP consist of four spherical probes on 50 inch booms as shown in the stowed position in fig. **??** along with the PIP, the SLP, and their common electronics enclosure. Each FPP instrument can be broken down into six subsections (see fig. **??**): 1) Probe, 2) Analog Front-End, 3) Analog Signal Conditioning, 4) Analog-to-Digital Conversion, 5) Digital Signal Processing, and 6) Telemetry Encoding. Detailed design schematics can be found in Appendix **??**. In this chapter we present the FPP design with expanded discussion of the sensors and each of these subsections of the instrument.

3.1 Probe

The FPP sensor was designed to be a 4-inch diameter, titanium nitrite coated, conducting sphere mounted approximately 3 inches from the end of each boom (see fig. **??**). Titanium nitrite was chosen for the surface finish because of its uniform work function. The tubing for the booms are made of glaspar epoxy fiberglass that is electrically insulated, stiff, and lightweight. On the other end of each boom is a locking hinge that has been designed and fabricated by UTD. Each boom is 50 inches long and weighs approximately 625 grams (including the hinges). When deployed, the four FPP booms are perpendicular to the spin axis of the payload and separated by 90^o. This separates each sensor by approximately 80 inches from the next one and by approximately 110 inches from the opposing one. There

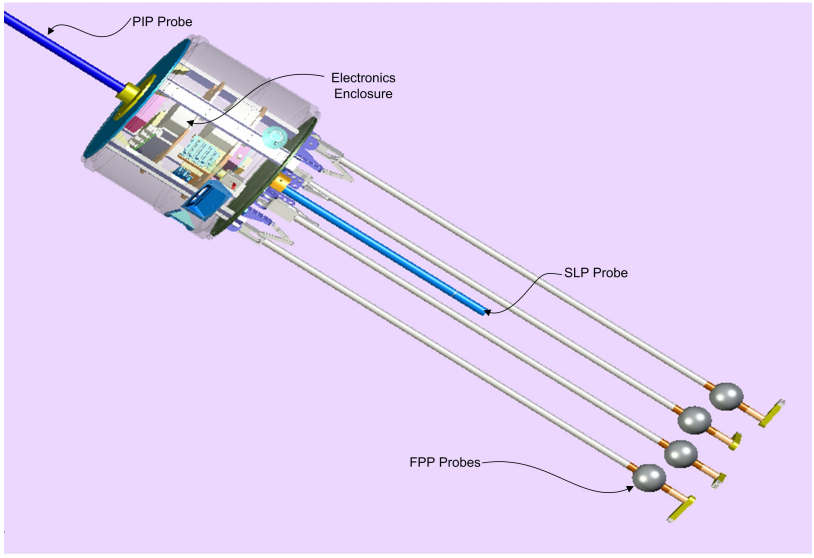

Fig. 3.1: FPP mechanical overview (FPP booms are shown in their stowed position).

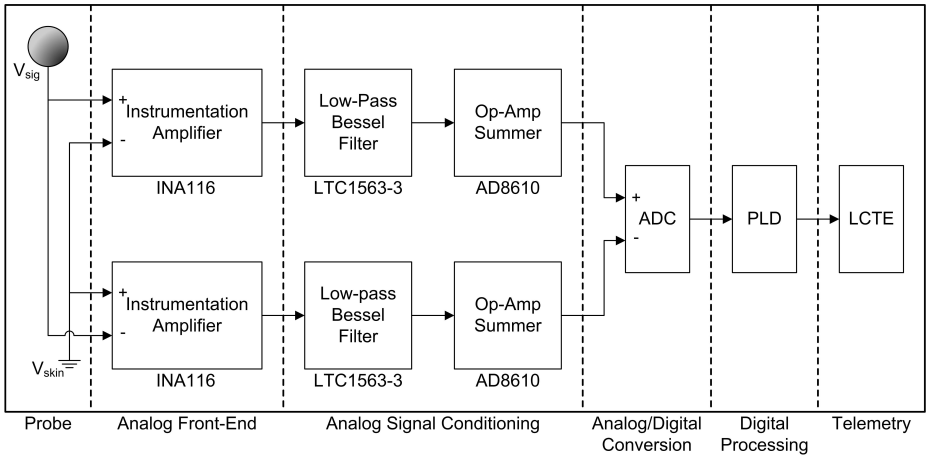

Fig. 3.2: Top-level block diagram of the FPP.

is a single coax cable that runs the length of each boom to connect the spheres to the FPP instrument.

3.2 Analog Front-End

The key to ensuring the success of the FPP instrument is found in the analog components that provide the electronic interface with the spherical sensors. It is vital that these components have a very high input impedance to ensure that the instrument will be able to take accurate measurements without disturbing the floating potential of the sensors.

The Storms FPP is implemented with a pair of instrumentation amplifiers to create a differential signal. Notice in fig. **??** that the input signal from the probe is connected to the positive terminal of one instrumentation amp and the negative terminal of the other instrumentation amp. The remaining negative and positive terminals are connected to the payload skin. This configuration provides a differential signal that is used for noise reduction in high-precision analog-to-digital conversion.

The INA116 manufactured by Texas Instruments was chosen as the instrumentation amp specifically for its extremely low input bias current (high input resistance). The INA116 is a completely monolithic FET-input instrumentation amplifier and utilizes Difet inputs and special guarding techniques to achieve an input bias current of 100fA max over a

Fig. 3.3: A FPP titanium nitrite coated sensor on the fiberglass boom mounted on the Storms subpayload.

temperature range of -40 to 85^oC. The input impedance is greater that $10^{15}\Omega$. Table **??** shows additional key characteristics.

In order to better understand the differential configuration of the FPP, a generic model of an instrumentation amplifier was developed using PSpice (see fig. **??**). The signal V_{src1} is connected to the positive terminal of the instrumentation amp and the signal V_{skin} is connected to the negative terminal (note that the positive and negative terminals of an instrumentation amp are determined by the differencing amp on the right not the op-amp buffers on the left). For clarity, this will be referred to as "positively configured." Not shown is a similarly configured instrumentation amp with V_{src1} connected to the negative terminal and V_{skin} connected to the positive terminal. This configuration will be referred to as "negatively configured." Also note that in a typical instrumentation amp configuration there is a resistor connected between the feedback loop inputs of the op-amps on the left. This resistor is used to set the gain of the instrumentation amp. For this application, the resistor is left floating in order to set the gain to unity for dynamic range purposes. In this example, V_{src1} is modeled as a sine wave with a 0.4V magnitude and a 2kHz frequency, V_{skin} is modeled as a sine wave with a 0.2V magnitude with a 20kHz frequency, and to show that AGND has no effect on the system, it was disturbed by a 50mV 100kHz sine wave. The top window of fig. **??** shows these inputs (note that there is a second input signal, V_{src2}, which will be discussed later). In this configuration, the output of the positively configured instrumentation amp is

$$V_{out1+} = V_{src1} - V_{skin} + \text{AGND}, \tag{3.1}$$

Table 3.1: INA116 parameters.

Parameter	Value
Input Offset Voltage	5mV max
Input Offset Voltage Drift	18μV/^{o}C max
Input Bias Current	100fA max (-40^{o}C to 85^{o}C) 150fA (125^{o}C)
Input Impedance	$\geq 10^{15}\Omega$
dc Common Mode Rejection Ratio	80dB min
Slew Rate	0.8V/μs typ
Settling Time to 0.1%	22μs typ (10V step)

and the negatively configure instrumentation amp output is

$$V_{out1-} = V_{skin} - V_{src1} + \text{AGND}. \tag{3.2}$$

These output are shown pictorially in the middle window of fig. **??**. Notice that the output signals contain all three sinusoidal "inputs." This differential configuration is required in order to reduce noise and utilize high-precision analog-to-digital converters (ADC). The bottom window of fig. **??** shows what the signal would look like after it is differenced in the ADC but before it is digitized. Mathematically, this is

$$V_{out1+} - V_{out1-} = 2\left(V_{src1} - V_{skin}\right). \tag{3.3}$$

Notice that the noise on the AGND signal dropped out of the final equation. This canceling out of any ground noise is also known as common mode rejection and is the reason high-precision ADC utilize differential signals. This signal is the floating potential of the payload.

Now suppose that there is a second FPP probe configured in the same way as the first but separated from the first by a distance, d. The output from this probe would be

$$V_{out2+} - V_{out2-} = 2\left(V_{src2} - V_{skin}\right). \tag{3.4}$$

During post-flight data analysis, the signals from these two probes can be differenced to produce

$$V_{out1+} - V_{out1-} - V_{out2+} + V_{out2-} = 2\left(V_{src1} - V_{src2}\right). \tag{3.5}$$

From the discussion in the previous chapter, it was shown that a knowledge of the voltage between two conduction probes in a plasma and the distance between them produces E-field measurements (see eq. (**??**)). Additionally, the two measurements can be summed together to provide insight into the floating potential of the spacecraft skin as discussed in sec. **??**.

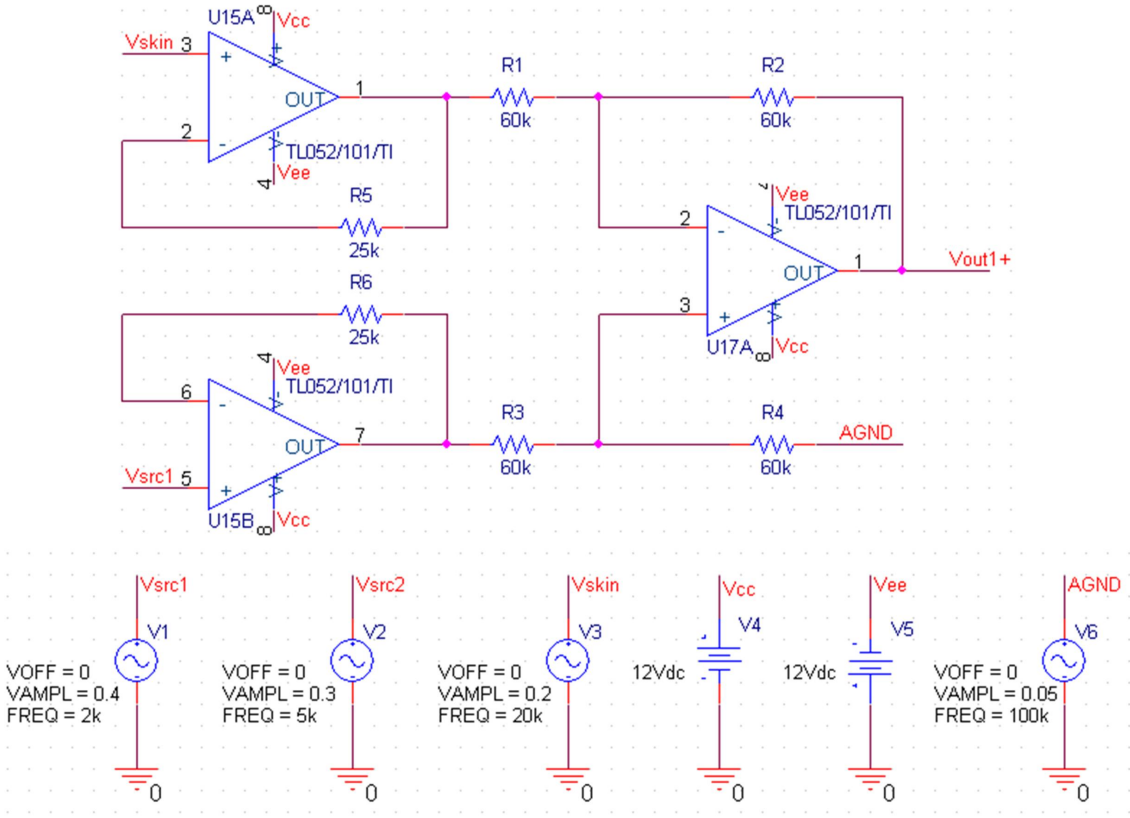

Fig. 3.4: PSpice instrumentation amp model.

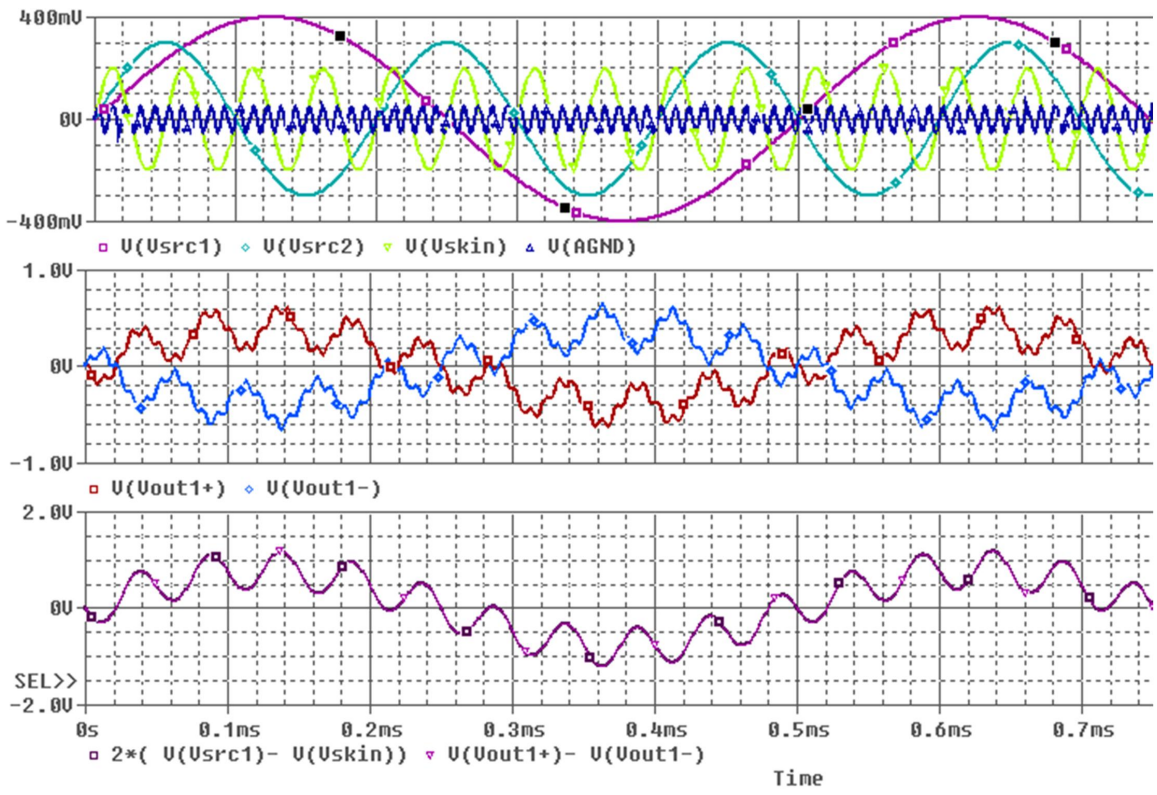

Fig. 3.5: PSpice instrumentation amp model outputs.

3.3 Analog Signal Conditioning and Digital Conversion

The output signal from the instrumentation amps require a small amount of signal conditioning before they can be passed to the ADC. This processing includes band-limiting the signal and shifting the signal to be in the range of the ADC.

3.3.1 Analog Filtering

The input to the FPP will be DC coupled and have a strong low-frequency component at the payload spin frequency. Therefore, it is important to be able to filter any spurious high-frequency noise while preserving the wave shape of the lower frequencies. This was accomplished with the use of a analog Bessel filter. These filters are characterized by a maximally flat group delay across the entire passband thus ensuring a low-noise low-frequency signal. For the Storms mission, this was implemented by using a analog Bessel filter chip, the LTC1563-3, manufactured by Linear Technology.

The LTC1563-3 is an active RC, 4th order, unity-gain, low-pass Bessel filter. It has rail-to-rail inputs and outputs, low DC offset, and features a low-power mode which is utilized in this application. It is also very simple to implement as one resistor value sets the cutoff frequency for the system ($R = 2.56 \times 10^9 \text{Hz}/f_c$). For this application a 1.3MΩ resistor was chosen giving a cutoff frequency of 2kHz. Table **??** shows additional characteristics.

3.3.2 Summer and ADC Driver Op-Amp

The last analog component the signal must pass through before it reached the ADC is a simple but very important op-amp. This op-amp provides the current to drive the ADC but it also conditions the signal for ADC processing. The ADC that was chosen for the Storms mission has a set of differential inputs with a 0 to 4.3V range. Therefore, the input signal has to be shifted from a -5 to 5 volt range to a 0 to 4 volt range. This was accomplished

Table 3.2: LTC1563-3 parameters.

Parameter	Value
Input Offset Voltage	6mV max
Input Offset Voltage Drift	$10\mu\text{V}/^o\text{C}$typ

by configuring the driving op-amp to also act as a non-inverting summer. Three resistors were added to the positive input of the op-amp to shift and gain the signal to within the correct ranges (see fig. **??**). The equation that describes this configuration is

$$V_{out} = \left(\frac{1}{10K} + \frac{1}{10K} + \frac{1}{20K}\right)^{-1} * \left(\frac{V_{in}}{10K} + \frac{5V}{10K} + \frac{0}{20K}\right) = \frac{2}{5}\left(V_{in} + 5\right). \tag{3.6}$$

The AD8610 is a very high precision JFET input amplifier manufactured by Analog Devices. Its characteristics include very low noise, low input bias current, and wide bandwidth making it ideal to drive the ADC. Table **??** shows the significant characteristics of this device.

3.3.3 Analog/Digital Conversion

Finally, the signal reaches the analog-to-digital converter. The selection of the ADC is critical because this device has to have a high sampling rate and a high resolution. A comparison of several ADCs revealed that the AD7678 manufactured by Analog Devices was the best available choice. It is a fully differential, 18-bit, 100 kSPS, charge redistribution SAR. It also has excellent accuracy with a maximum integral nonlinearity of 2.5 LSB with no missing 18-bit codes. The other parameters of the AD7678 are shown in Table **??**.

3.4 Digital Processing

After the signal is digitized, it is sent to the FPGA that is shared between the FPP and the Sweeping Langmuir Probe. The FPGA is a Altera Cyclone part number EP1C12F256C7.

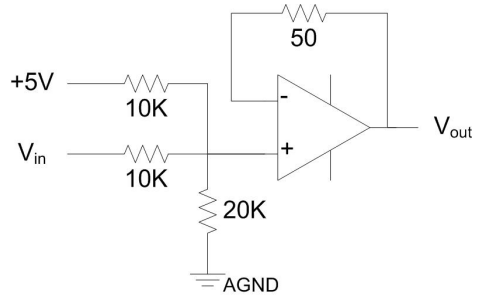

Fig. 3.6: Configuration of the current driving and summing op-amp.

Table 3.3: AD8610 parameters.

Parameter	Value
Input Offset Voltage	850μV max
Input Offset Voltage Drift	3.5μV/^{o}Ctyp
Input Bias Current	250pA max (-40^{o}C to 85^{o}C) 2.5nA (125^{o}C)
Input Offset Current	75pA max (-40^{o}C to 85^{o}C) 150pA (125^{o}C)
dc Common Mode Rejection Ratio	90dB min
Slew Rate	50V/μs typ
Gain Bandwidth Product	25MHz
Settling Time to 0.01%	350ns typ (4V step)

Table 3.4: AD7678 parameters.

Parameter	Value
Integral Linearity Error	$\pm$2.5 LSB max
Differential Linearity Error (No Missing Codes)	18 Bits
Zero Error	$\pm$40 LSB max (-40^{o}C to 85^{o}C)
Gain Error	$\pm$0.048% max of FSR
Temperature Drift	$\pm$0.5ppm/^{o}C typ Zero Error $\pm$1.6ppm/^{o}C typ Gain Error
Input Impedance	Very High
Internal Reference Voltage	4.096V
SN+D	200dB typ
THD	-118dB typ
Full Linear Bandwidth	900kHz
Sample and Hold Amplifier	2ns typ Delay 5ps rms typ Jitter 8.5μs max Transient Response

The FPGA performs several important functions for the FPP instrument. First, it ensures that the inputs from all four FPP instruments are sampled simultaneously. This is critical to producing accurate e-field measurements because now the differencing between the probes occurs during data analysis. Second, the FPGA co-adds and averages every eight samples to produce a 20-bit measurement and to reduce noise. Lastly, the FPGA receives commands from the LCTE board and outputs the data for transmission to the ground station.

3.5 Telemetry Design

After each signal has been co-added and averaged they are sent via a backplane within the electronics box to the LCTE board for transfer to ground. Each instrument on the Storms daughter payload has its own telemetry requirements as discussed in sec. **??**. Figure **??** shows the details of each data channel where the Sample Rate is samples per seconds and is determined by the spatial resolution required, the Word Size is the number of bits in each sample, the Words/Sample is the number of measurements in a sample, and the Bit and Word Rates are the number of bits and words required per second.

All of the data channels along with the various NASA attitude, location, and housekeeping channels are organized to produce the telemetry matrix which is shown, in part, in fig. **??**. A major frame is defined as 64 minor frames each of which has 32 16-bit words. The overall telemetry bit rate is 2.5 MHz resulting is a major frame rate of about 76.3 Hz.

Columns 4-9 and 20-25 depict the data channels of the PIP, namely, the SIP, PFP, and DCP, respectively. The SIP is sampled twice every minor frame and results in real and imaginary absolute impedance measurements, real and imaginary impedance minus the free space capacitance measurements, and absolute impedance magnitude measurements. Also, the free space capacitance is recorded once every major frame. Multiplexing the PFP results in a 32-bit word that is divided into the low-order and high-order bits and sampled once every two minor frames. The DCP provides both a high-gain and low-gain measurement and is sampled once every other minor frame.

Columns 2-3, 10-11, 18-19, and 26-27 are the SLP data channels labeled LG and HG. Due to the possibility that the SLP will dramatically change the floating potential of the

Channel	Label	Sample Rate (Hz)	Word Size (Bits)	Words/ Sample	Bit Rate (Bits/s)	Word Rate (Word/s)
DCP Low Gain	DCPL	2441.4	16	1	39062.5	2441.4
DCP High Gain	DCPH	2441.4	16	1	39062.5	2441.4
PFP Low Bits	PFPH	2441.4	16	1	39062.5	2441.4
PFP High Bits	PFPL	2441.4	16	1	39062.5	2441.4
SIP Impedance Magnitude	SIPM	76.3	16	128	156250.0	9765.6
SIP Impedance Real Total	SIPR	76.3	16	128	156250.0	9765.6
SIP Impedance Imaginary Total	SIPI	76.3	16	128	156250.0	9765.6
SIP Impedance Real Delta	SIPRD	76.3	16	128	156250.0	9765.6
SIP Impedance Imaginary Delta	SIPID	76.3	16	128	156250.0	9765.6
SIP Free Space Capacitance	Co	76.3	16	1	1220.7	76.3
PIP Housekeeping	PIP	76.3	16	16	19531.3	1220.7
SLP High Gain	HG	38.1	16	512	312500.0	19531.3
SLP Low Gain	LG	38.1	16	512	312500.0	19531.3
FPP Sensor 1	VS1	4882.8	16	1	78125.0	4882.8
FPP Sensor 2	VS2	4882.8	16	1	78125.0	4882.8
FPP Sensor 3	VS3	4882.8	16	1	78125.0	4882.8
FPP Sensor 4	VS4	4882.8	16	1	78125.0	4882.8
FPP Least Significant Bits	Vlsb	4882.8	16	1	78125.0	4882.8
SLP/FPP Housekeeping	SLP	76.3	16	15	18310.5	1144.4
NASA GPS	GPS	4882.8	16	1	78125.0	4882.8
NASA Magnetometer	A2, A3, A4	1220.7	16	3	58593.8	3662.1
NASA Housekeeping	Axx	152.6	16	24	58593.8	3662.1
NASA Time Event	T1A, T2A	152.6	16	2	4882.8	305.2
Spare	Spare	4577.6	16	1	73242.2	4577.6
TM Overhead	SFID, SYNC	14648.4	16	1	234375.0	14648.4
				Total	2,500,000.0	156,250.0

Fig. 3.7: Telemetry overview for the Tropical Storm Mission.

	1	2	3	4	5	6	7	8	9	10	11	12	13	14	15	16
1	SFID	LG	HG	SIPR	SIPRD	SIPI	SIPID	SIPM	DCPH	LG	HG	V1S	V2S	V3S	V4S	Vlsb
2									DCPL							
3																
4																
5																
6																
57																
58																
59																
60																
61																
62																
63	↓	↓	↓	↓	↓	↓	↓	↓	DCPH	↓	↓	↓	↓	↓	↓	↓
64	SFID	LG	HG	SIPR	SIPRD	SIPI	SIPID	SIPM	DCPL	LG	HG	V1S	V2S	V3S	V4S	Vlsb

	17	18	19	20	21	22	23	24	25	26	27	28	29	30	31	32
1	GPS	LG	HG	SIPR	SIPRD	SIPI	SIPID	SIPM	PFPL	LG	HG	A1	A3	T1A	SYNC	SYNC
2									PFPH			PIP	A0	T1B		
3												A2	A4	Spare		
4												SLP	A5			
5												A1	A3			
6												PIP	A6			
58												PIP	A25			
59												A2	A26			
60												SLP	A28			
61												A1	A3			
62												PIP	A29			
63	↓	↓	↓	↓	↓	↓	↓	↓	PFPL	↓	↓	A2	A30	↓	↓	↓
64	GPS	LG	HG	SIPR	SIPRD	SIPI	SIPID	SIPM	PFPH	LG	HG	Co	A31	Spare	SYNC	SYNC

Fig. 3.8: PCM matrix for the Tropical Storms Mission.

payload skin and thereby interfering with the FPP measurements, the SLP performs one 512-point sweep every twenty seconds and is otherwise held at a constant 3 volts. This data is captured in four high-gain and four low-gain samples that are symmetrically sampled each minor frame.

The FPP channels are depicted in columns 12-16 labeled VS1, VS2, VS3, VS4, and Vlsb. Through co-adding, each FPP instrument produces a 20-bit word which results in the 16 high-order bits of each instrument being transmitted as VS1, VS2, VS3, and VS4 and the four low-order bits of each sample being concatenated together and transmitted as Vlsb. The four low-order bits for FPP1 are located at the four highest bit locations within Vlsb. The four low-order bits for FPP2 and FPP3 follow respectively with the four low-order bits for FPP4 located in the four lowest bit locations within Vlsb. The four FPP probes are simultaneously sampled once per minor frame.

The remaining channels include the sub-frame IDs and the synchronization words, the housekeeping data, and NASA data. The housekeeping data includes temperature monitors and voltage monitors. The NASA samples record GPS, attitude, and timing data.

3.6 Gain and Resolution

The overall gain of the system can be seen by considering the gain of each component. The instrumentation amps and Bessel filters both have unity gain. The driving op-amp set the gain of each signal to $0.4V_{in}$ with an offset of 2 to condition the signal for digital conversion. The ADC is differential meaning the output is the "positive" input minus the "negative" input with respect to the ADC. The overall gain of the system is

$$(0.4V_{in} + 2) - (0.4(-V_{in}) + 2 \Rightarrow 0.8V_{in}. \tag{3.7}$$

However, the input signal has also now become digitized. The ADC is an 18-bit converter with a 8.192V range (-4.096 to 4.096) meaning that each bit is equal to $31.25\mu V$. In the FPGA, the samples are co-added and averages resulting in a 20-bit sample with each bit

equal to $7.8125\mu V$. Conversion from input voltage V_{in} to counts is

$$\text{Counts} = \frac{0.8V_{in} + 4.096}{7.8125 \times 10^{-6}}. \tag{3.8}$$

Ideally, the conversion of counts back to volts would be the inverse of eq. (**??**) which is

$$\frac{1}{0.8}(7.8125 \times 10^{-6}\text{Counts} - 4.096). \tag{3.9}$$

3.7 Printed Circuit Board

The properties and layout of the Printed Circuit Board (PCB) were also taken into consideration. Due to the high input impedance required by the FPP, the PCB material had to restrict the leakage of current through the board. Rogers 4350 was used because it has a volume resistivity of 1.2×10^{10}. The board was also configured with special attention paid to trace locations and lengths. The layout of the PCB is shown in fig. **??** and the layout schematics can be found in Appendix **??**. The FPP connector, located at the bottom of the picture, was procured from ITT Canon and is part number DCM21XA4PJK87. It is configured with four coax connectors and 17 single pin connectors. The coax connectors were used for the inputs to the FPP instrument and the single pin connectors were used for test and calibration. Just above the FPP connector is the row of instrumentation amplifiers followed by a row of Bessel filters and a row of driving op-amps and ADCs. On the right side of the board is the SLP instrument. Near the middle of the PCB is the FPGA with other miscellaneous chips to the left of the FPGA. At the top of the board is the backplane connector.

3.8 Electronics Enclosure

The electronics enclosure is where all of the USU built electronics are housed for the Storms Mission. It contains four PCBs each mounted in a stainless steel tray (see figs. **??** and **??**). The circuit boards are (from top to bottom): the PIP instrument, the SLP/FPP instrument, the Low-Cost Telemetry Encoder (LCTE) board, and the Power board. Each

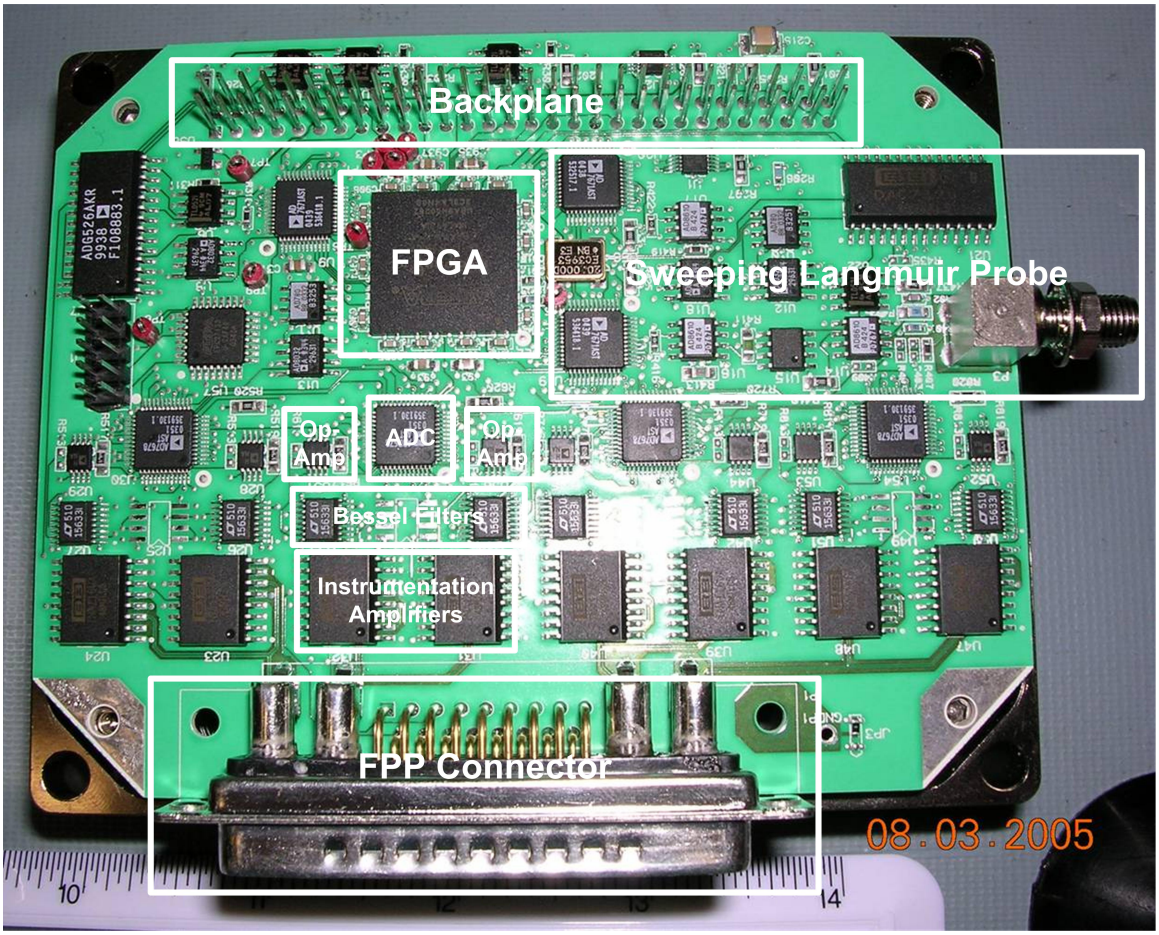

Fig. 3.9: Picture of the FPP PCB.

PCB is 4.5in x 3.5in and varies between 6 to 10 layers thick. The dimensions of the entire stack is 4.7in L x 3.75in W x 3.32in H. To reduce electromagnetic interference between boards, each board is separated by a nickel-plated aluminum shield 50 mils thick. Each board is required to have a interconnecting header that enables each board to communicate with the other boards via a common backplane. This allows the stack to easily expand as necessary and negates the need for a separate backplane board thus miniaturizing the stack.

The PIP board is required to be at the top of the stack to place it close to the PIP boom and keep the cables connecting the two as short as possible. The board has two external connectors which are placed on the front of the stack. One is a triax connector that ties the PIP instrument to the SIP/PFP section of the boom. The other is a D-sub connector that has five coax connectors and 12 signal pins. The coax connectors are used to connect the DC instrument to the DCP section of the boom and the signal pins are used for instrument calibration.

The SLP/FPP board is just under the PIP board and also has two external connectors. The D-sub connector is mounted on the front of the stack and has four coax connectors and 17 signal pins. Each coax connector is used to connect the FPP instrument to one of the FPP spheres and the signal pins are used for calibration and grounding purposes. On the left side of the stack is a SMA coax connector that ties the SLP instrument to the SLP probe.

The LCTE board is next underneath the SLP/FPP board and has a 110-pin SMA connector mounted on the front of the stack. It is able to convey both analog and digital telemetry signals to the transmitter for transmission to the ground station. The power board is located at the bottom of the stack and provides appropriate voltage regulation given an input voltage of 12-60 VDC through its 20-pin SMA connector.

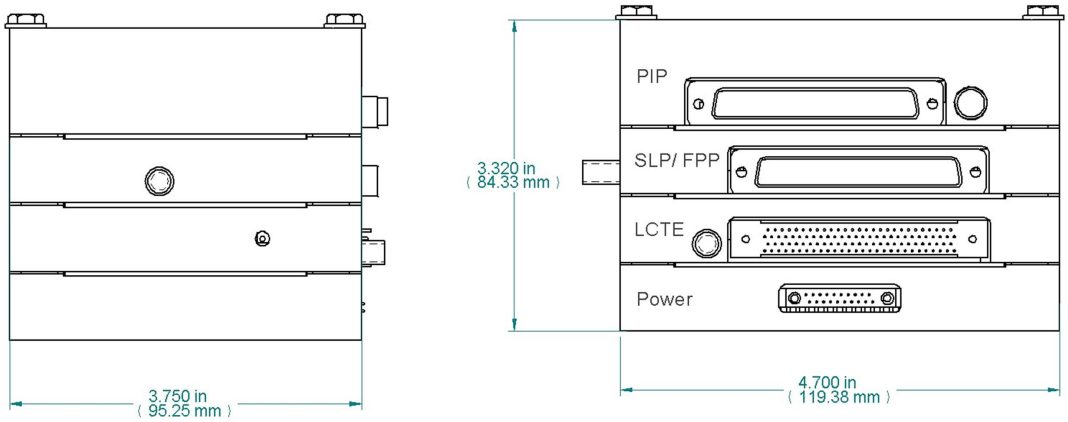

Fig. 3.10: Schematic of the Storms Mission Electronics Enclosure.

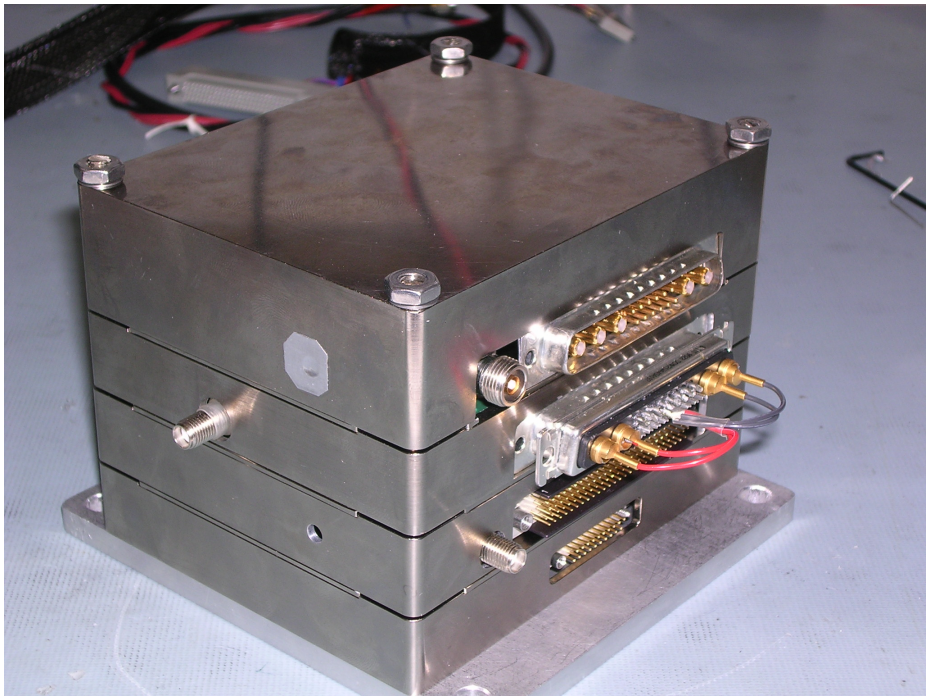

Fig. 3.11: Picture of the Storms Mission Electronics Enclosure.

Chapter 4

FPP Testing and Calibration

The FPP underwent a series of tests to prove its functionality, accuracy, and validity. Tests were conducted to measure the DC noise magnitude, input impedance, the frequency response, and the saturation recovery response of each instrument. From this series of tests, a set of calibrations were developed for the FPP. This chapter will discuss the method and results of each of these tests.

4.1 Test Method

Testing of the FPP instrument was controlled via LabView. The LabView card was able to request data directly from the PLD on the SLP/FPP board through the calibration pins on the D-sub connector or it can request data from the LCTE board while the LCTE talks to the FPP instrument through the backplane.

4.2 DC Noise Test

The DC Noise Test was the first test performed on the FPP and served two purposes by not only showing the DC noise of the system but also showing that the instrument was functional. This test was executed by applying a DC voltage on the input of the instrument and observing the output. The input stepped from -5VDC to 5VDC in approximately 0.5VDC increments. A very low-noise DC input was created using a 9V battery and a number of resistors and switches configured on an electronic bread board. The exact input was measured using a voltmeter at the input to the FPP and the output was observed in counts using LabView. This test was conducted several times in different configurations (see Table **??**).

Table 4.1: DC test configurations.

Run	Date	Input Signal	Voltmeter	Calibration Port/LCTE	Board Location
1	25 May 06	Battery	Fluke	LCTE	Bottom
2	25 May 06	Voltage Standard	Keithley	LCTE	Bottom
3	30 May 06	Battery	Keithley	LCTE	Bottom
4	13 Jun 06	Battery	Fluke	Cal Port	Bottom
5	14 Jun 06	Battery	Fluke	LCTE	Bottom
6	14 Jun 06	Battery	Fluke	LCTE	Top
7	14 Jun 06	Battery	Fluke	LCTE	Top
8	15 Jun 06	Battery	Fluke	LCTE	Bottom
9	09 Aug 06	Battery	Fluke	Cal Port	Top
10	09 Aug 06	Battery	Fluke	LCTE	Top

The first test was set up using the battery/resistor configuration to provide a quiet DC input, a Fluke voltmeter to measure the input voltage, a LCTE board (serial number 2) for telemetry, and with the FPP board on the bottom of a stack of circuit boards (the power board and the LCTE board being on top) in semi-enclosed in a stainless steel tray. The power was turned on to the electronics stack and the LabView script was used to control the test. The input from the battery/resistor network was applied to each of the the input connectors of the FPP instrument. Then the input voltage was measured by the voltmeter at the connector and was recorded. The voltmeter was then removed from the circuit and the LabView script was then triggered to take samples for approximately 1 second and store the data. In this way, all four FPP channels were tested simultaneously. A switch was flipped on the battery/resistor network board which provided for another DC step and the test was repeated. The stored data from LabView was imported into a Matlab script and used in conjunction with the recorded input voltages to process the data and create fig. **??**. Figure **??** shows the standard deviation for each of the 4 FPP instruments. For this test the standard deviation was typically between 3-5 counts with the highest deviation being near 8 counts. These 8 counts translate into having 3-bit error within a 20-bit word or, in other words, the FPP has 17-bit resolution.

This DC test procedure was executed at least 10 different times, some with slightly different set up configurations. After the first test was run, the battery/resistor network

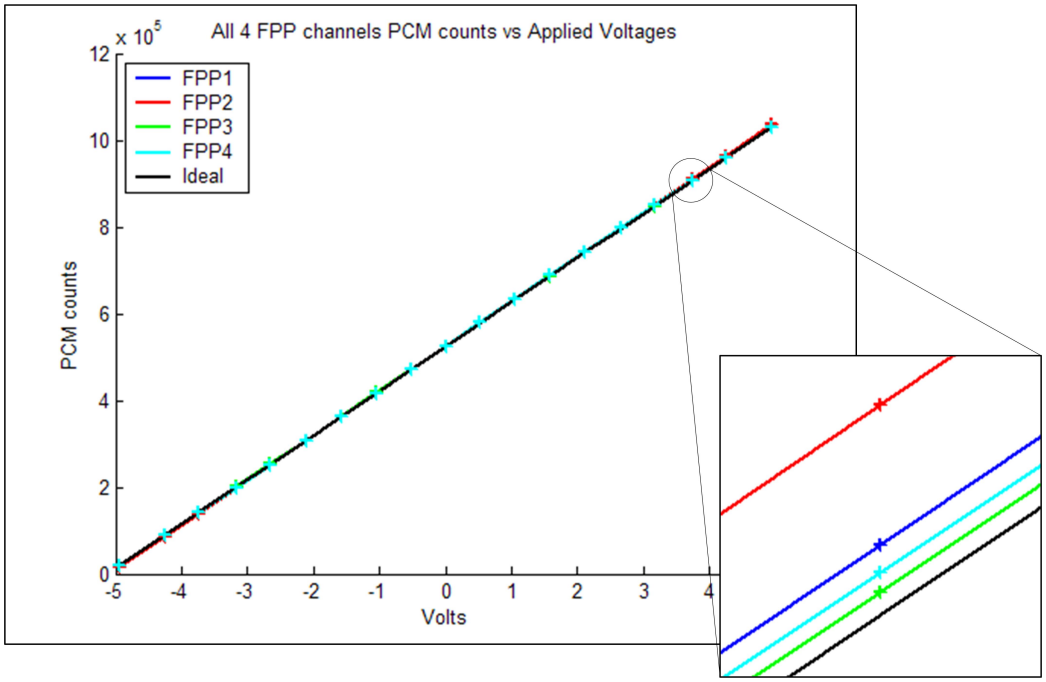

Fig. 4.1: This figure shows the input voltage vs. PCM counts for the first DC test of the FPP.

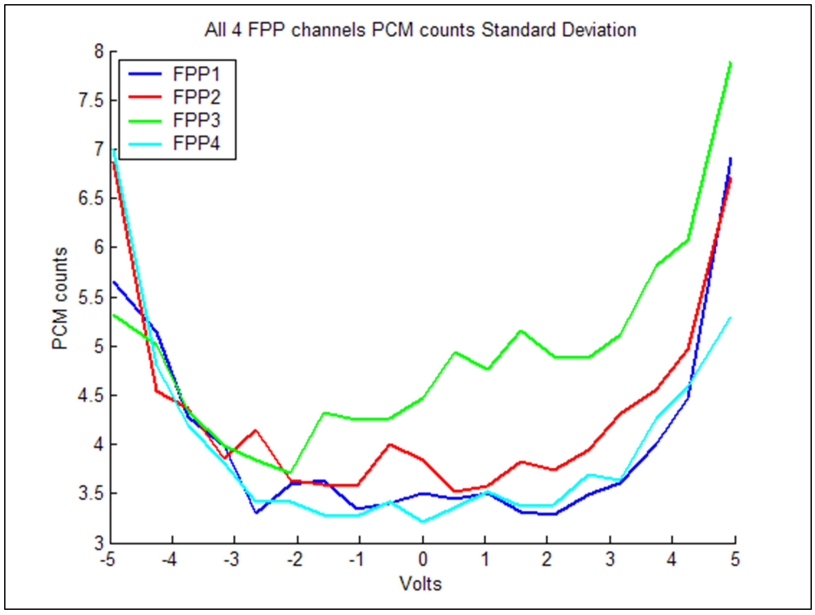

Fig. 4.2: This figure shows the standard deviation for the first DC test of the FPP.

was swapped for a voltage standard. However, the voltage standard was considerably more noisy than the battery/resistor network and was therefore not used again. At the same time, the Fluke volt meter was swapped for a Keithley volt meter. The Keithley provided more precision to the input voltage measurement. However, there was some debate about how long it had been since the Keithley had been calibrated. Also during the test, the DC battery source had a observable decay which made the extra precision invalid because it kept changing anyway. Another variation between the tests was the output source of the data. There were two tests conducted that used the calibration port to retrieve the data as opposed to going through the LCTE and the LabView script. This resulted in much higher DC noise on the FPP due to the cross talk between the signal coming though the analog portion of the instrument and the output calibration lines which ran right underneath the analog portion of the instrument. There was also two different LCTE boards used for this test, LCTE 2 and LCTE 3. However, there was no observable difference between the two boards. The last variation between the tests, was the location of the board. Initially, the FPP electronics board was placed at the bottom of the stack with the LCTE and the power boards located on top. After doing some work on the SLP side of the board, it was reasoned that the board should be placed above the power and the LCTE boards to more closely resemble flight configuration. This proved to be a bad idea due to the low-frequency noise created by the florescent lighting in the lab. This is a non-issue during flight because the circuit boards will all be enclosed. Therefore, the best configuration was one in which the battery/resistor network was used to produce the necessary quiet DC input voltage, the Fluke voltmeter measured the input voltage, the data was recorded though the LCTE/LabView setup, and the FPP board was located at the bottom of the stack of electronic boards to protect it from additional noise. Test numbers 1, 5, and 8 were conducted in this manner and the similarities between these three tests can be easily seen by comparing the collected data subtracted from an ideal curve. These results can be seen in fig. **??**.

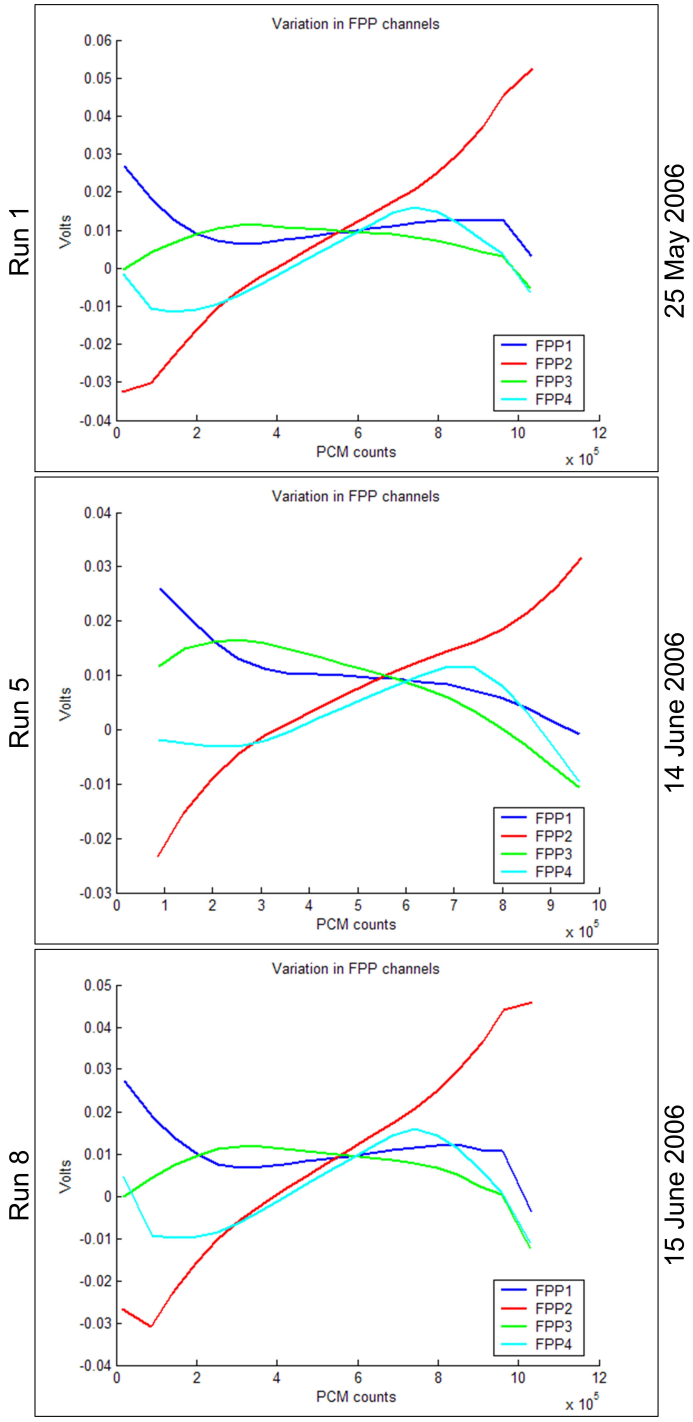

Fig. 4.3: This figure shows the similarities between DC test runs 1, 5, and 8.

The data from the DC test can also be used to convert PCM counts back into volts (see sec. **??**).

4.3 Input Impedance

After verifying that the FPP instrument was functional and had acceptable DC gain and noise, the next step was to measure the input impedance of each FPP instrument. The instrumentation amplifiers on the input of the FPP were specially chosen because of their very high input impedance, about $10^{15}\Omega$. This test it implemented by attaching a small charged capacitor to the input of the instrument and observing the rate of decay of the current from the capacitor through the FPP instrument (see fig. **??**). The data was collected through the LCTE board using a LabView script that was set to collect data for about 5 minutes. Ideally, the equation that governs the rate of decay is

$$i = V_{in} \exp^{-t/RC} . \tag{4.1}$$

For this test, the capacitor was charged using a voltage supply to 5 volts. The capacitor values chosen for this test were 100 pF and 10 pF. Using eq. (**??**) the output current of the FPP instrument should look like the blue line in fig. **??** for the 100pF capacitor and like the red line for the 10pF capacitor.

In a non-ideal situation, there are a couple other factors that play into this scenario. First, the typical impedance of the air near the circuit board can affect the rate of decay. The resistance of air varies due to humidity and other factors but typically can be estimated to be in the 10^{10} to $10^{11}\Omega$ range. In other words, the resistance of air is 1000 to 10,000 time less than the input impedance of the instrument. These two resistances can be thought of as being in parallel, and therefore the lower resistance would control the decay rate of the capacitor. Another factor is the people in the room. Amazingly, as people moved about the room as the test was being conducted it changed the capacitance of the surrounding environment and there were noticeable differences in the rate of decay as someone moved closer to or farther from the test. In the end, the test had to be conducted while there was

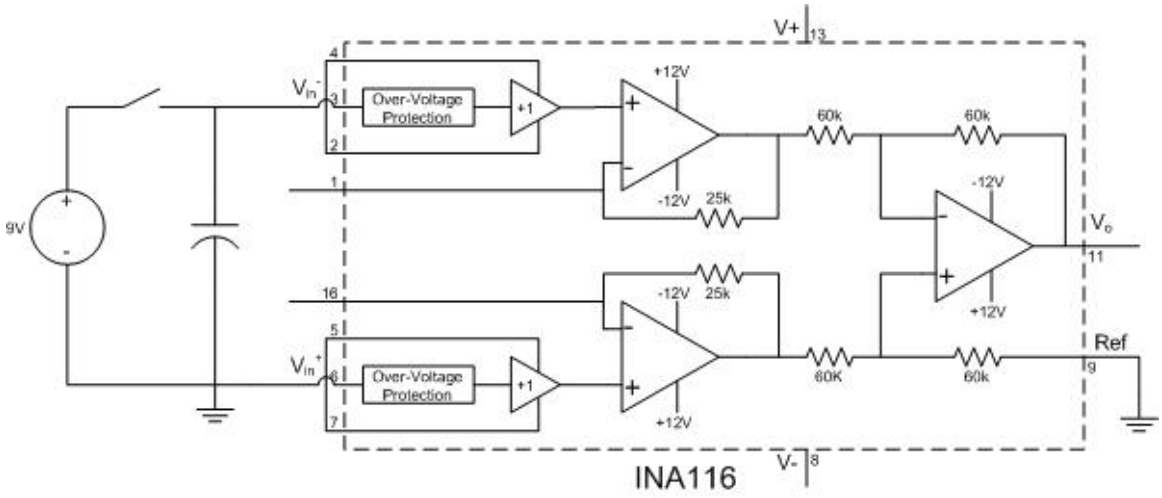

Fig. 4.4: Setup of FPP input impedance test.

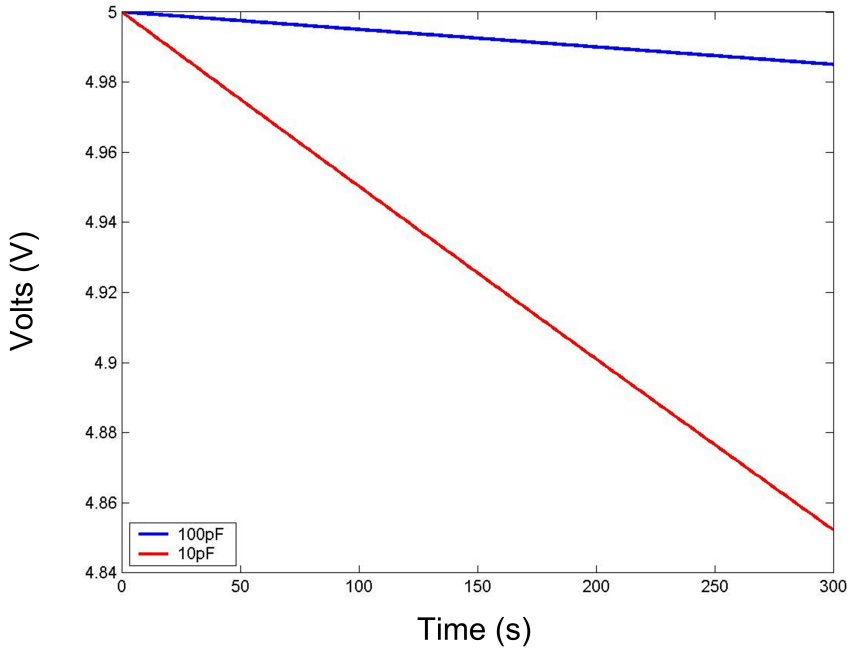

Fig. 4.5: This figure shows the ideal rate of decay for a 100pF (blue) capacitor and a 10pF (red) capacitor with a $10^{15}\Omega$ resistor and a 5V input voltage.

only one person in the room and that person had to sit very still for the duration of the test.

The results of the test are shown in figs. **??** and **??**. In these figures, the blue, red, green, and black lines show the results for FPP1, FPP2, FPP3, and FPP4, respectively. The magenta, yellow, and cyan plots show the ideal curves for a 10^{13}, 10^{14}, and 10^{15} Ω input resistance. By comparing the slope of the measured curves against the slope of the ideal curves the approximate input impedance can be determined. These plots show that the input impedance that was imposed on the capacitor was somewhere between 10^{13} and $10^{14}\Omega$.

4.4 Frequency Response

The FPP also underwent a series of test to show the frequency response of each instrument. This test was set up by using a sine wave generator to produce a -4V to 4V sine wave input for a range of frequencies. The frequencies chosen for this test ranged from 100Hz to 20kHz. The frequencies from 100Hz to 3kHz stepped in 100Hz increments and from 3kHz to 20kHz in 1kHz increments. The output from the FPP was recorded using the LCTE board and the LabView interface. Figure **??** shows the results of this test (small discontinuities are the result of having to run the tests over smaller frequency ranges) which shows that the low-pass Bessel filter does indeed have a cutoff frequency of 2kHz.

4.5 Saturation Recovery Test

The last test performed on the FPP was conducted to get an idea of the saturation recovery response of the instrument. This test was conducted by simply putting a low-frequency sinusoidal wave at the input of the instrument and measuring the output using LCTE and LabView. In this case, however, the magnitude of the sine was was intentionally set to exceed the input ranges of the FPP. Figure **??** shows a 12Vpp 1Hz sinusoidal input and the response of the FPP. Note that the instrument recovers from saturation almost without delay. This figure also shows the range of the FPP. A closer looks reveals that the instrument becomes saturated between -4.93 and -4.96 on the negative side and between

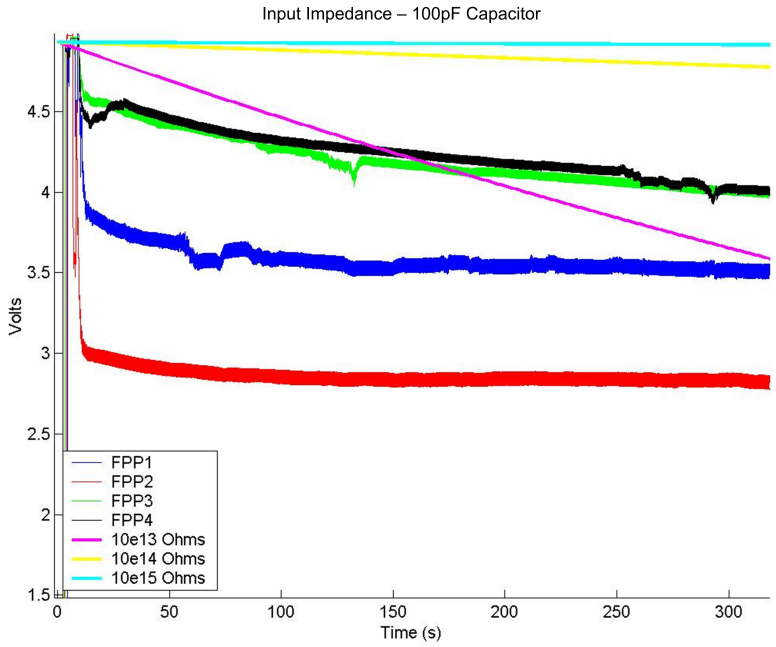

Fig. 4.6: Results of the input impedance test using a 100pF capacitor.

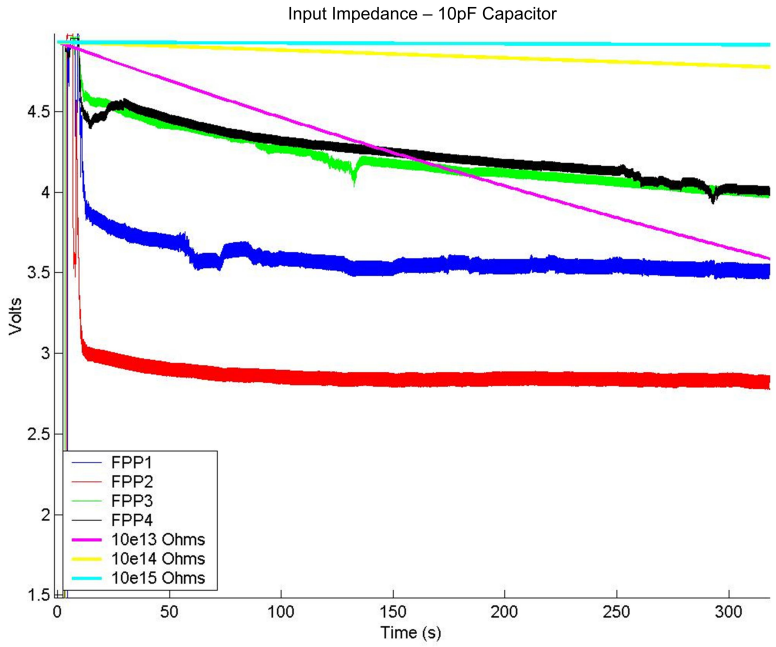

Fig. 4.7: Results of the input impedance test using a 10pF capacitor.

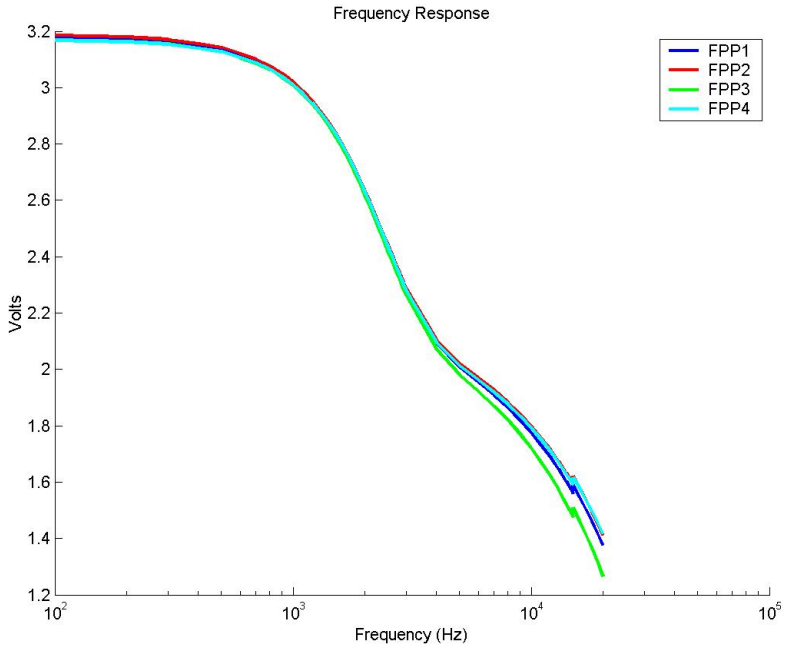

Fig. 4.8: Frequency response of the FPP instrument.

4.93 and 4.96 on the positive side. This shows that the instrument is functional over almost the entire range from -5 to 5 volts.

4.6 Calibration

Calibration of the FPP involves reconciling the slight offset from the ideal of each FPP (see fig. **??**) to zero. This is accomplished by one of two methods. The first method is to fit a polynomial to each offset curve and use that polynomial as the calibration for each channel. The second method is to interpolate between the points of each offset curve and use that as the calibration. Each method has its merits.

4.6.1 Polynomial Curve Fit

Inspection of the offset curves indicate that a 3rd order polynomial would most likely produce a good fit. The actual polynomial fits are shown in figs. **??**, **??**, **??**, and **??**. The error between the offset and the polynomial fit for each channel is shown in fig. **??**. As

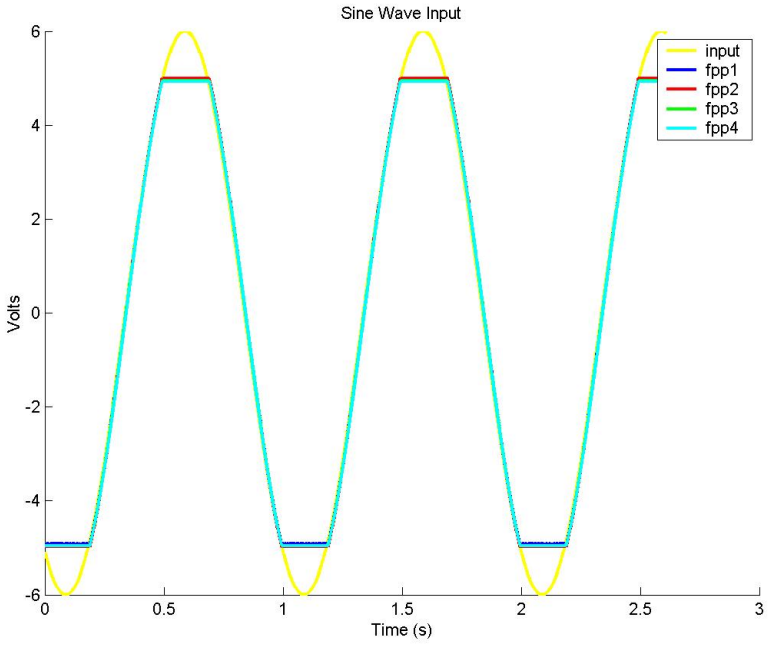

Fig. 4.9: FPP response to a 12Vpp 1Hz Sinusoidal signal. Note the performance of the FPP as it enters into and recovers from saturation.

shown, the error for a 3rd order polynomial is ±4mV. The coefficients for the polynomial are shown in Table **??**.

4.6.2 Interpolation

The second method for calibration is to perform interpolation on the offset curves. Given the computing tools available, it is reasonably simple to use the 19 data points taken as part of the DC Noise Test as the error and interpolate between them to produce the required data. For Run 1, these data points are shown in Table **??**.

Table 4.2: 3rd order polynomial fit coefficients.

$ax^2 + bx + c$	a	b	c
FPP1	-0.0050	0.0027	0.0070
FPP2	0.0031	0.0005	0.0189
FPP3	0.0003	-0.0045	-0.0017
FPP4	-0.0078	-0.0041	0.0199

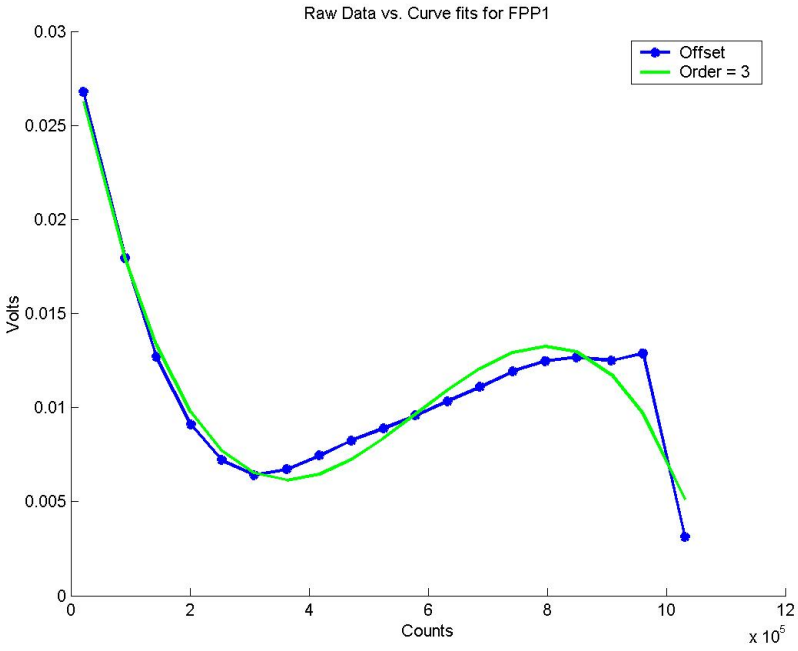

Fig. 4.10: FPP1 offset curve and 3rd order polynomial fit.

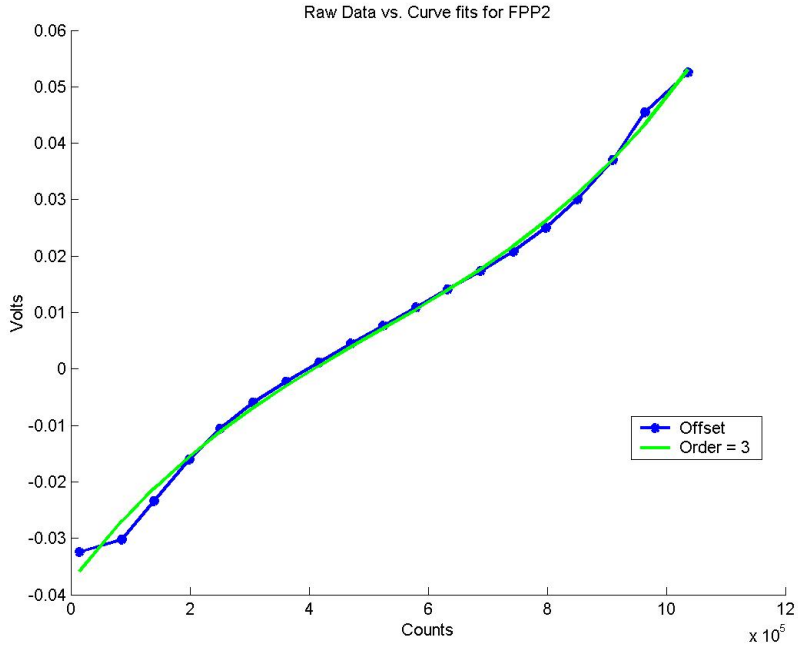

Fig. 4.11: FPP2 offset curve and 3rd order polynomial fit.

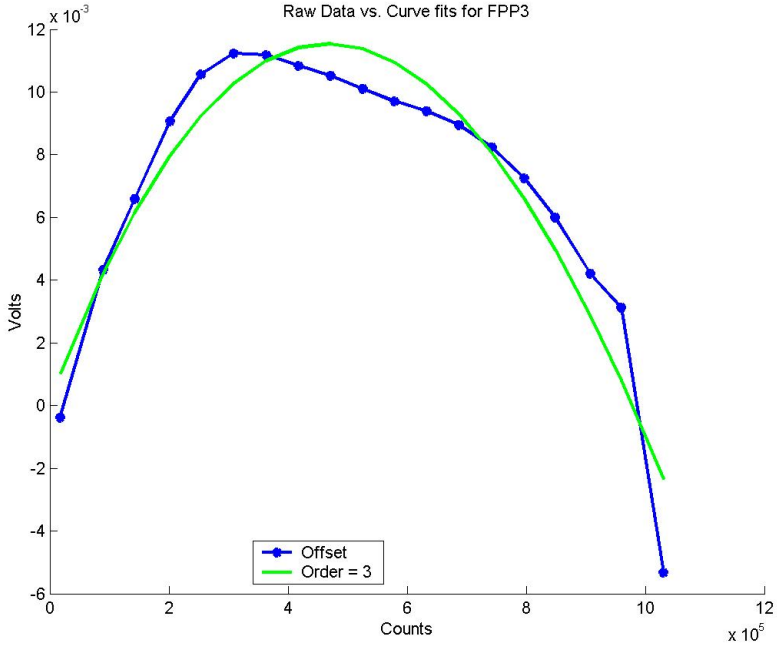

Fig. 4.12: FPP3 offset curve and 3rd order polynomial fit.

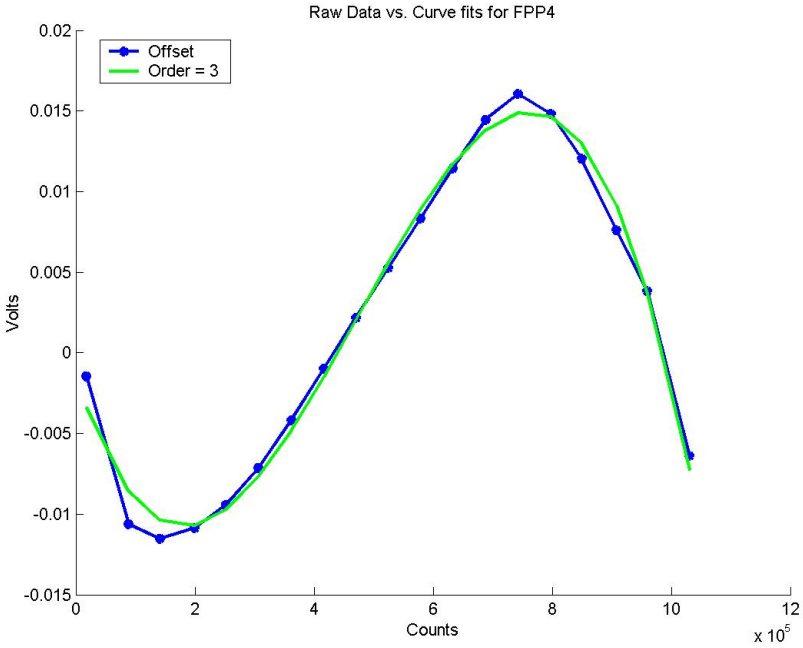

Fig. 4.13: FPP4 offset curve and 3rd order polynomial fit.

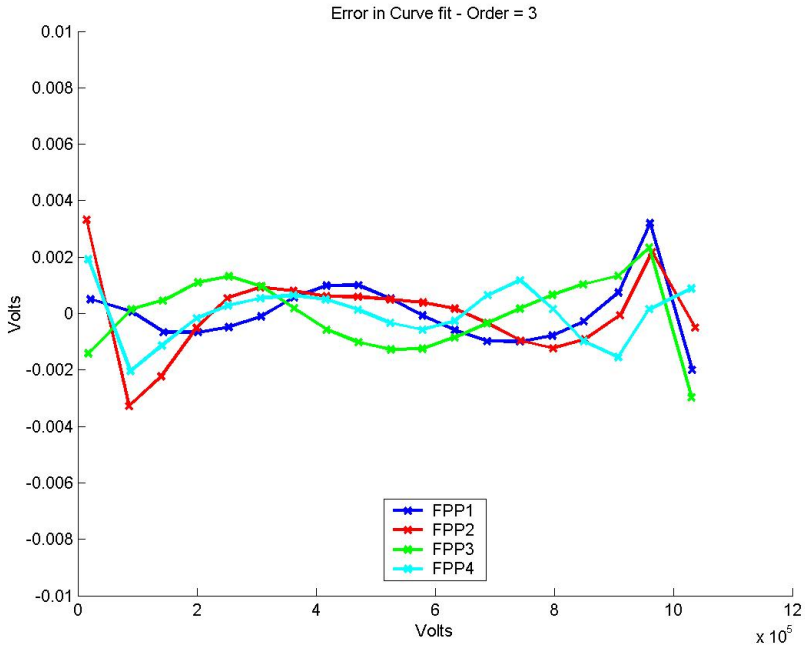

Fig. 4.14: The difference between the actual offset and the 3rd order polynomial curve fit for each channel.

Table 4.3: Interpolation calibration data points.

Input	FPP1	FPP2	FPP3	FPP4
-4.9450	0.026777	-0.032490	-0.000388	-0.001457
-4.2489	0.017956	-0.030187	0.004323	-0.010609
-3.7336	0.012699	-0.023404	0.006597	-0.011534
-3.1592	0.009101	-0.016037	0.009055	-0.010870
-2.6531	0.007217	-0.010556	0.010553	-0.009443
-2.1175	0.006405	-0.005929	0.011238	-0.007138
-1.5810	0.006718	-0.002210	0.011185	-0.004190
-1.0496	0.007450	0.001150	0.010839	-0.001007
-0.5274	0.008244	0.004475	0.010519	0.002155
0.0001	0.008888	0.007672	0.010103	0.005253
0.5278	0.009582	0.010894	0.009696	0.008336
1.0505	0.010336	0.014114	0.009397	0.011440
1.5818	0.011097	0.017313	0.008949	0.014442
2.1185	0.011922	0.020785	0.008234	0.016045
2.6543	0.012469	0.025031	0.007243	0.014802
3.1608	0.012684	0.030104	0.006000	0.012027
3.7360	0.012488	0.037080	0.004212	0.007613
4.2511	0.012881	0.045516	0.003130	0.003832
4.9500	0.003119	0.052523	-0.005325	-0.006391

Chapter 5

Conclusion

5.1 Performance

At the beginning of this project, the direction was given to design and build an instrument that would be able to take measurements of the floating potential of the spacecraft and also produce accurate E-field measurements. The specific requirements for the FPP are:

1. A very high input impedance - greater than 10^{10}.
2. The gain of the system must be very accurately known.
3. Filter out high-frequency noise.
4. Minimum resolution is 16 bits.
5. Interface with the LCTE board through the common backplane.
6. Compatible with the power supply board.
7. Physically fit within the pre-designed electronics stackup.

From the tests performed as described in Chapter 4, it has been shown that the instrument works very well as a high-precision volt meter and will be able to take accurate measurements of the ionospheric environment. The input impedance test has shown that the FPP has an input impedance on the order of 10^{13} to $10^{14}\Omega$ range (see figs. **??** and **??**). The analog components for the FPP have been specifically chosen and configured to very accurately set the gain of the system to $0.8V_{in}$. The frequency response (see fig. **??**) has shown that the Bessel low-pass filter is set to 2kHz. Finally, the DC Noise test has

shown that the DC noise of the system is sufficiently low enough (see fig. **??**) to produce 17 or more good bits of data within each sample taken. This instrument communicates well with the telemetry board, receives power from the power board and fits nicely within the electronics stack.

5.2 Lessons Learned

One major design error of the FPP is that is was assumed that differential ADC means that the ADC accepts negative voltage inputs. This is not the case. The input range of the instrument usually has to be scaled to meet the input requirements of the ADC. Another problem resulted because high frequency signal traces (such as calibration port signals) were placed beneath the analog components of the FPP. This caused problems with retrieving clean data from the calibration port but was not a major concern since the test and calibration data could be retrieved via the backplane. In short, many other minor problems with this instrument could have been avoided if more attention had been paid to the data sheets. Also, an end-to-end model of the instrument developed at the beginning of the design process would have been useful both for understanding the big picture and also for avoiding and troubleshooting problems.

All in all, the fabrication, assembly, and test of the PCB went fairly smoothly. One minor issue was that one batch of PCBs failed a test performed at the PCB manufacturer. The failure happened because one of the board layers was offset a few thousandths of an inch further than what was permitted. Unfortunately, the results of these tests were not submitted to SDL until after one of these failed boards had been assembled. The board was tested and it was determined that there was no short between the layers and would be acceptable for flight. Another problem was the quality of work done at the SDL Surface Mount Lab. The FPP had to be double and triple checked for loose parts and hidden globs of solder each time there was any work done on it. Lastly, the FPP inputs are sensitive to electrostatic discharge and a special grounding connector was made to ensure that the sensitive inputs were always grounded when not in use.

5.3 Future Work

The Tropical Storms mission was launched from Wallops Flight Facility, VA on October 30, 2007. Due to the long delay between the initial integration of the FPP and the actual flight window, the instrument had to be checked, tested, and re-calibrated again before flight. The work forward from this point involves performing the data analysis and redesigning the instrument for future flights. The data from the Storms mission needs to be analyzed and compared to what was expected and to the data from the other instruments on the mission. Lastly, the current circuit board has many patches and quick-fixes. The instrument needs to be redesigned for future flights using the lessons learned.

Fig. 5.1: Tropical Storms Mission Launch.

References

[1] Living with a Star, "Layers of the ionosphere," http://ds9.ssl.berkeley.edu/LWS_GEMS/6/secf_9a.htm, 2006.

[2] D. Hastings and H. Garrett, *Spacecraft-Environment Interactions*. The Edinburgh Building, Cambridge CB2 2RU, UK: Cambridge University Press, 1996.

[3] M. C. Kelley, "In situ ionospheric observations of severe weather-related gravity waves and associated small-scale plasma structure," *Journal of Geophysical Research*, vol. 102, pp. 329–334, Jan. 1997.

[4] A. Hummel, "The plasma impedance probe: A quadrature sampling technique," Master's thesis, Utah State University, Logan, 2006.

[5] J. A. Henry, "Implementation of a user-configurable low cost telemetry encoder," Master's thesis, Utah State University, Logan, 2004.

[6] T. B. Campbell, "Low-cost telemetry encoder backplane communication," Master's thesis, Utah State University, Logan, 2006.

[7] C. G. Carlson, "Next generation plasma frequency probe instrumentation technique," Master's thesis, Utah State University, Logan, 2004.

[8] R. F. Pfaff, *In-situ Measurement Techniques for Ionospheric Research*. Greenbelt, Maryland, USA: NASA/Goddard Space Flight Center, 1996.

[9] A. Pedersen, F. Mozer, and G. Gustafsson, "Electric field measurements in a tenuous plasma with spherical double probes," in *Measurement Techniques in Space Plasmas*, R. F. Pfaff, J. E. Borovsky, and D. T. Young, Eds. Washington, DC: American Geophysical Union, 1998, pp. 1–12.

[10] N. C. Maynard, "Electric field measurements in moderate to high density space plasmas with passive double probes," in *Measurement Techniques in Space Plasmas*, R. F. Pfaff, J. E. Borovsky, and D. T. Young, Eds. Washington, DC: American Geophysical Union, 1998, pp. 13–28.

Appendices

Appendix A

Design Schematics

The following drawings (fig **??**) are the schematic drawing of USU-FPP as designed in Mentor Graphics.

Connectors

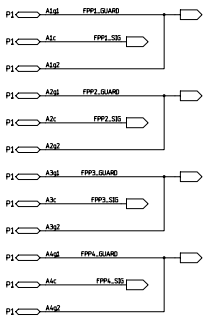

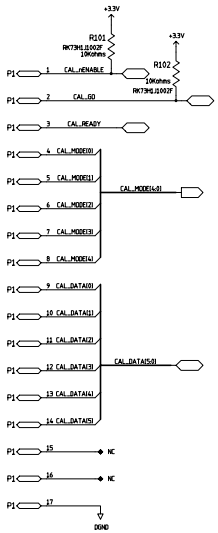

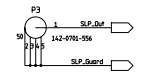

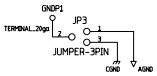

PROGRAM: Tropical Storm	SPACE DYNAMICS LABORATORY UTAH STATE UNIVERSITY RESEARCH FOUNDATION North Logan, Utah 84341				
NEXT ASSEMBLY					
NEXT ASSY TITLE	TITLE: External Interface				
ENGINEER: J Gregory	SCHEMATIC NAME: Schematic1	INSTANCE NAME:	DRAWING NUMBER: 61-0010		SCH REV: -
LAST MODIFIED: 6/27/2005	SCHEMATIC: OF	INSTANCE: OF	SCH-INST SHEET: 01 OF 10	TOTAL SCHEMATIC PAGES: 1 OF 10	

Form No. QF0412 Rev D

Power

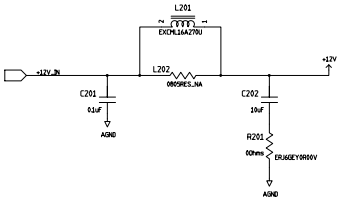

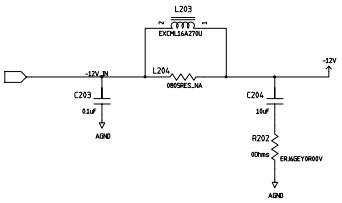

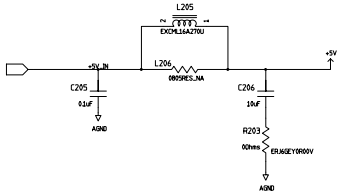

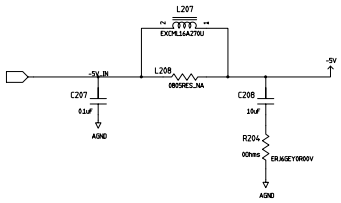

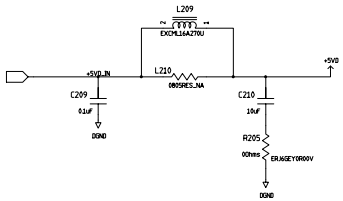

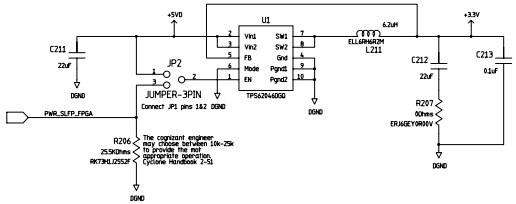

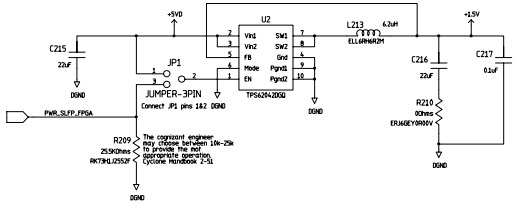

PROGRAM: Tropical Storm	SPACE DYNAMICS LABORATORY UTAH STATE UNIVERSITY RESEARCH FOUNDATION North Logan, Utah 84341				
NEXT ASSEMBLY					
NEXT ASSY TITLE	TITLE: Power				
ENGINEER: J Gregory	SCHEMATIC NAME: Schematic1	INSTANCE NAME:	DRAWING NUMBER: 61-0010		SCH REV: -
LAST MODIFIED: 6/27/2005	SCHEMATIC: OF	INSTANCE: OF	SCH-INST SHEET: 02 OF 10		TOTAL SCHEMATIC PAGES: 2 OF 10

House Keeping

Voltage Monitors

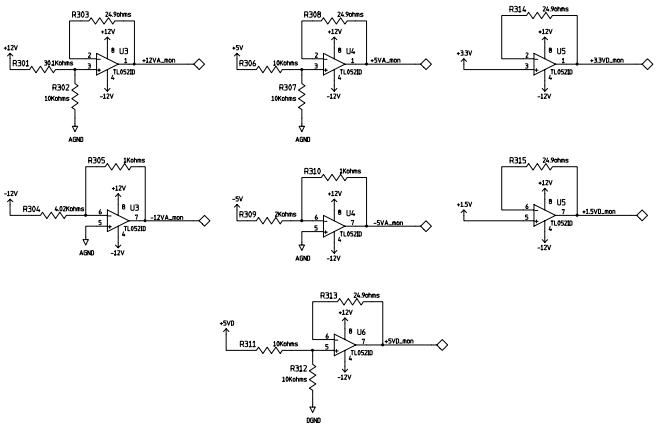

ADC

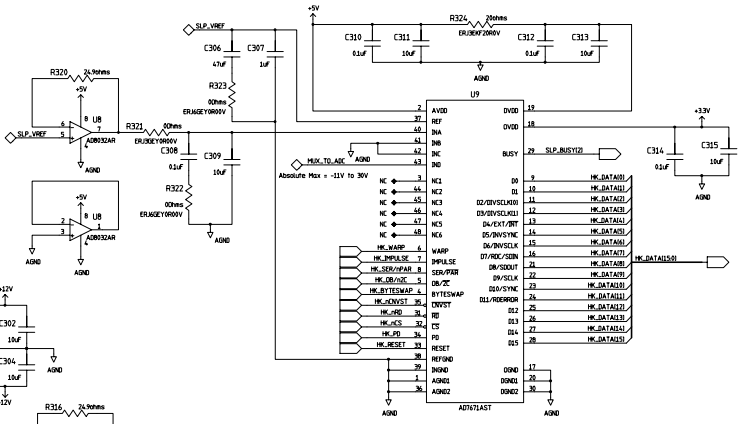

MUX

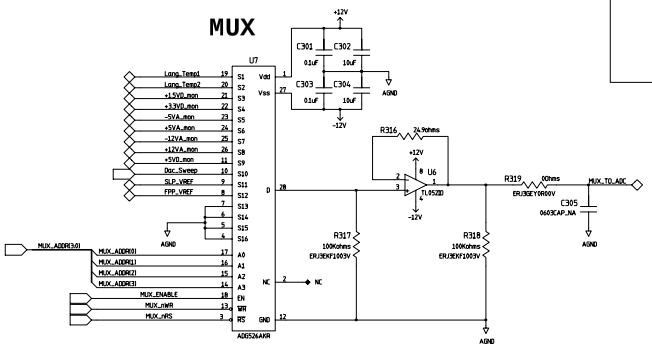

Decoupling for U3 / U4 / U5 / U6 / U8 / U12 / U13

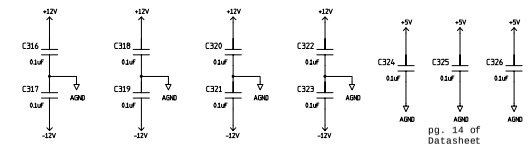

pg. 14 of Datasheet

Temperature Sensors and Voltage Reference

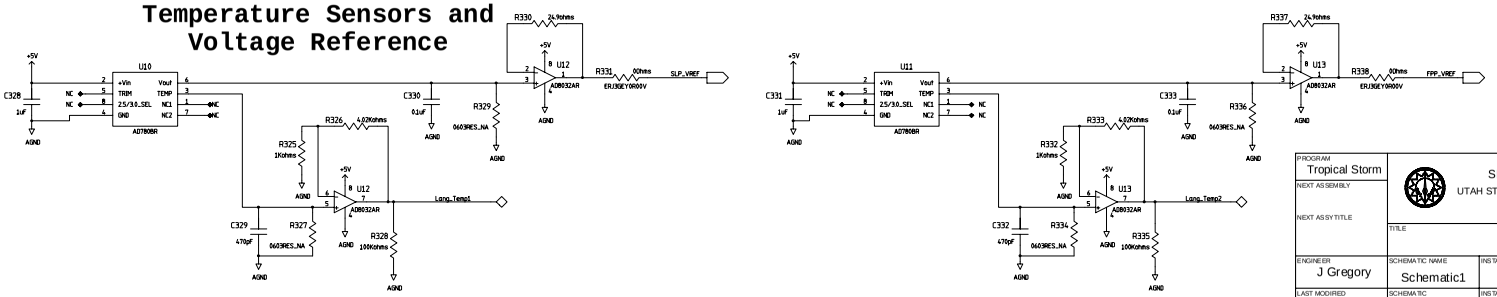

PROGRAM: Tropical Storm	SPACE DYNAMICS LABORATORY UTAH STATE UNIVERSITY RESEARCH FOUNDATION North Logan, Utah 84341				
NEXT ASSEMBLY					
NEXT ASSY TITLE	TITLE: House Keeping				
ENGINEER: J Gregory	SCHEMATIC NAME: Schematic1	INSTANCE NAME:	DRAWING NUMBER: 61-0010		SCH REV: -
LAST MODIFIED: 6/27/2005	SCHEMATIC: OF	INSTANCE: OF	SCH-INST SHEET: 03 OF 10		TOTAL SCHEMATIC PAGES: 3 OF 10

Sweeping Langmuir Probe Interface

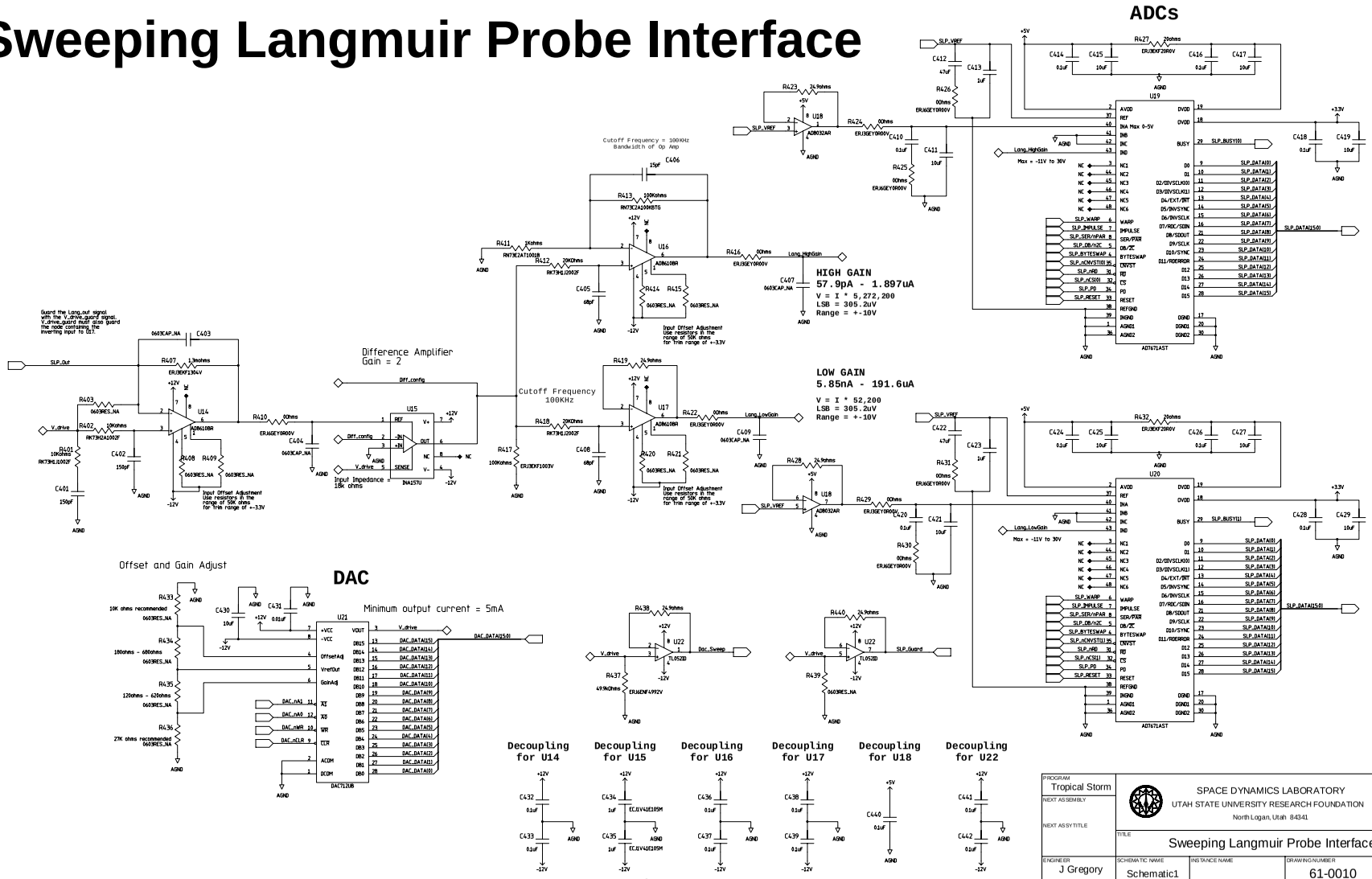

PROGRAM: Tropical Storm	SPACE DYNAMICS LABORATORY UTAH STATE UNIVERSITY RESEARCH FOUNDATION North Logan, Utah 84341				
NEXT ASSEMBLY					
NEXT ASSY TITLE	TITLE: Sweeping Langmuir Probe Interface				
ENGINEER: J Gregory	SCHEMATIC NAME: Schematic1	INSTANCE NAME:	DRAWING NUMBER: 61-0010		SCH REV: -
LAST MODIFIED: 6/27/2005	SCHEMATIC: OF	INSTANCE: OF	SCH-INST SHEET: 04 OF 10		TOTAL SCHEMATIC PAGES: 4 OF 10

Floating Potential Probe 1 Interface

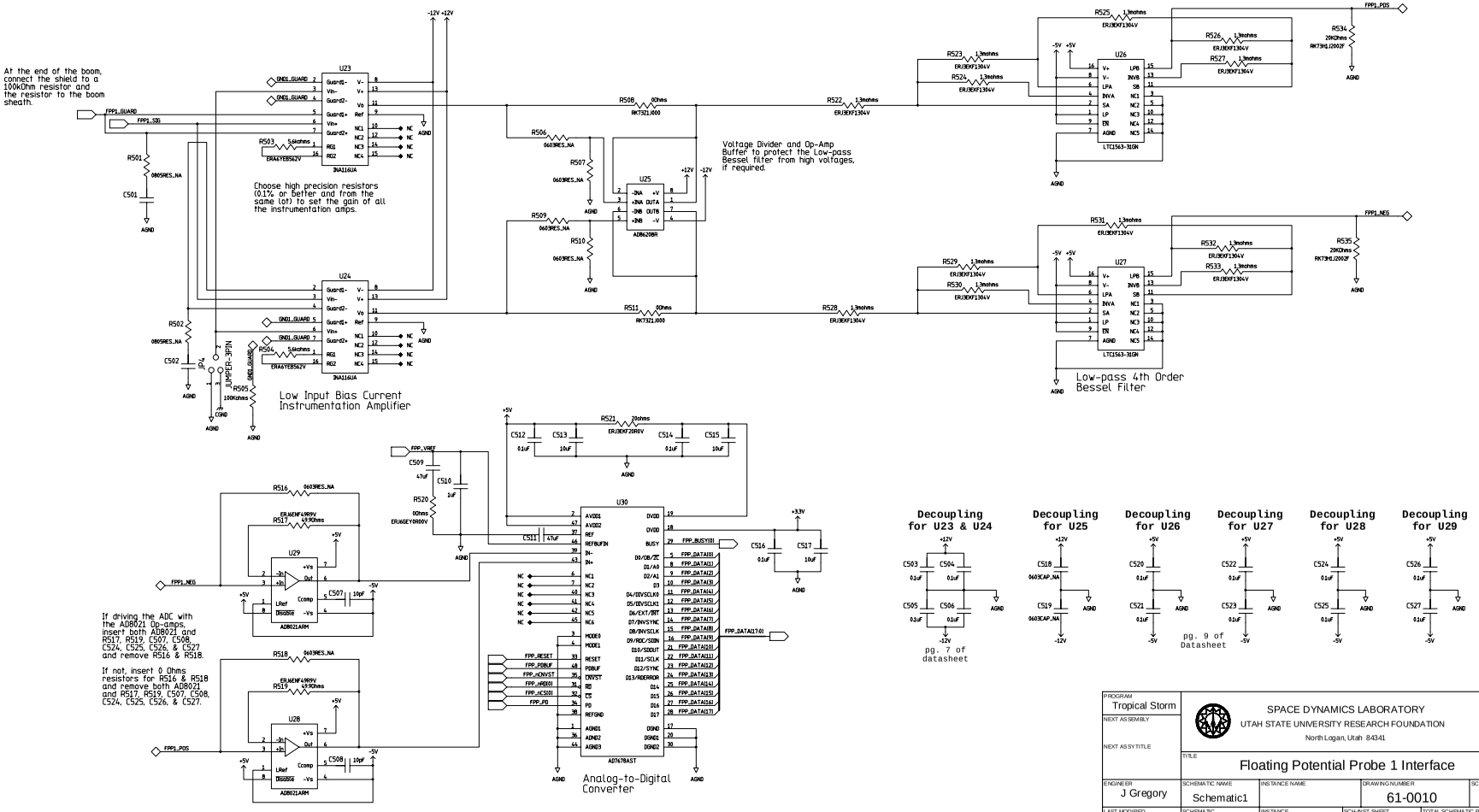

PROGRAM: Tropical Storm	SPACE DYNAMICS LABORATORY, UTAH STATE UNIVERSITY RESEARCH FOUNDATION, North Logan, Utah 84341				
NEXT ASSEMBLY	TITLE: Floating Potential Probe 1 Interface				
NEXT ASSY TITLE					
ENGINEER: J Gregory	SCHEMATIC NAME: Schematic1	INSTANCE NAME	DRAWING NUMBER: 61-0010	SCH REV: -	
LAST MODIFIED: 6/27/2005	SCHEMATIC: OF	INSTANCE: OF	SCH-INST SHEET: 05 OF 10	TOTAL SCHEMATIC PAGES: 5 OF 10	

Form No. QF0412 Rev D

Floating Potential Probe 2 Interface

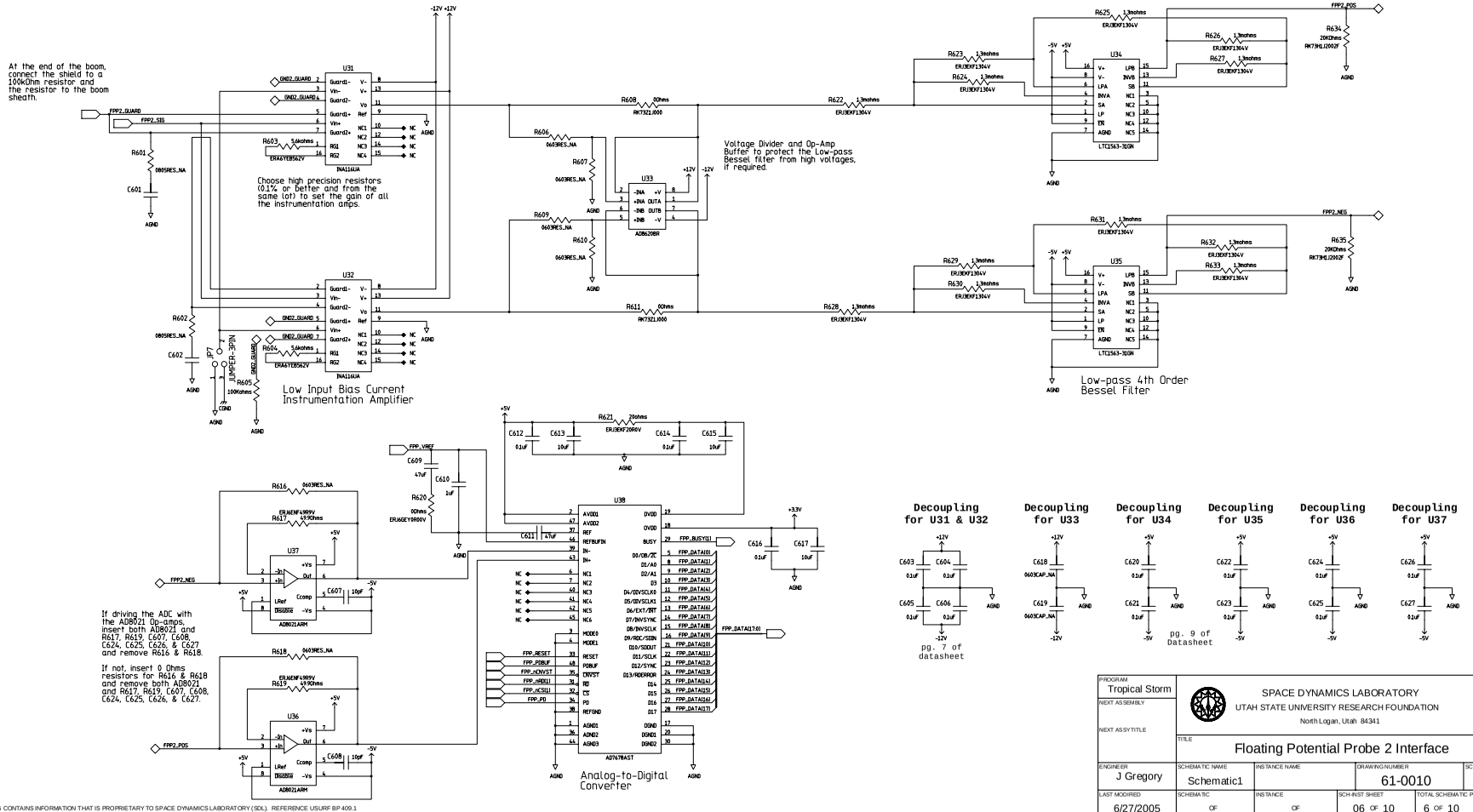

PROGRAM: Tropical Storm	SPACE DYNAMICS LABORATORY UTAH STATE UNIVERSITY RESEARCH FOUNDATION North Logan, Utah 84341				
NEXT ASSEMBLY	TITLE: Floating Potential Probe 2 Interface				
NEXT ASSY TITLE					
ENGINEER: J Gregory	SCHEMATIC NAME: Schematic1	INSTANCE NAME:	DRAWING NUMBER: 61-0010	SCH REV: -	
LAST MODIFIED: 6/27/2005	SCHEMATIC: OF	INSTANCE: OF	SCH-INST SHEET: 06 OF 10	TOTAL SCHEMATIC PAGES: 6 OF 10	

Form No. QF0412 Rev D

Floating Potential Probe 3 Interface

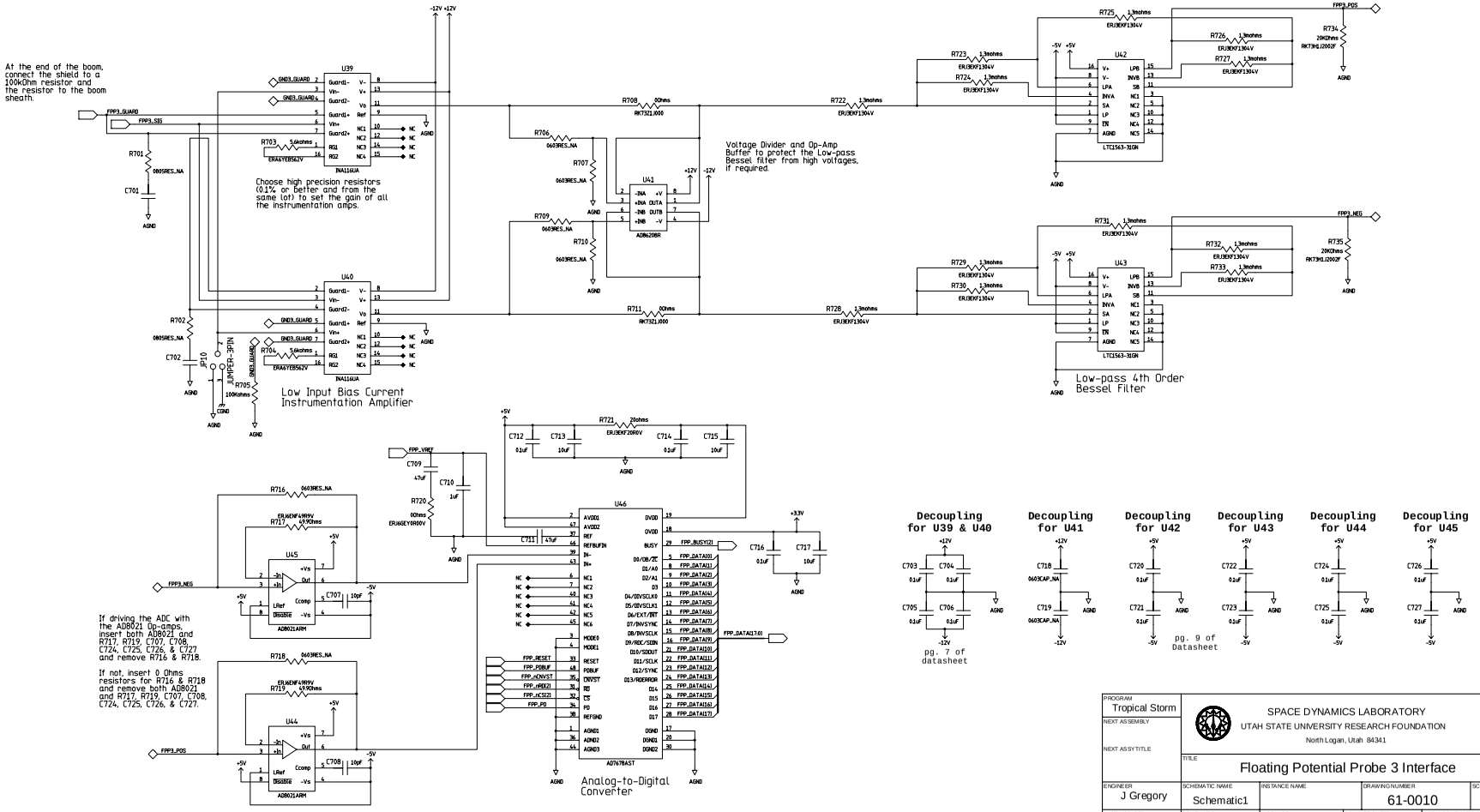

PROGRAM: Tropical Storm	SPACE DYNAMICS LABORATORY, UTAH STATE UNIVERSITY RESEARCH FOUNDATION, North Logan, Utah 84341				
NEXT ASSEMBLY	TITLE: Floating Potential Probe 3 Interface				
NEXT ASSY TITLE					
ENGINEER: J Gregory	SCHEMATIC NAME: Schematic1	INSTANCE NAME:	DRAWING NUMBER: 61-0010	SCH REV: -	
LAST MODIFIED: 6/27/2005	SCHEMATIC: OF	INSTANCE: OF	SCH-INST SHEET: 07 OF 10	TOTAL SCHEMATIC PAGES: 7 OF 10	

Form No. QF0412 Rev D

Floating Potential Probe 4 Interface

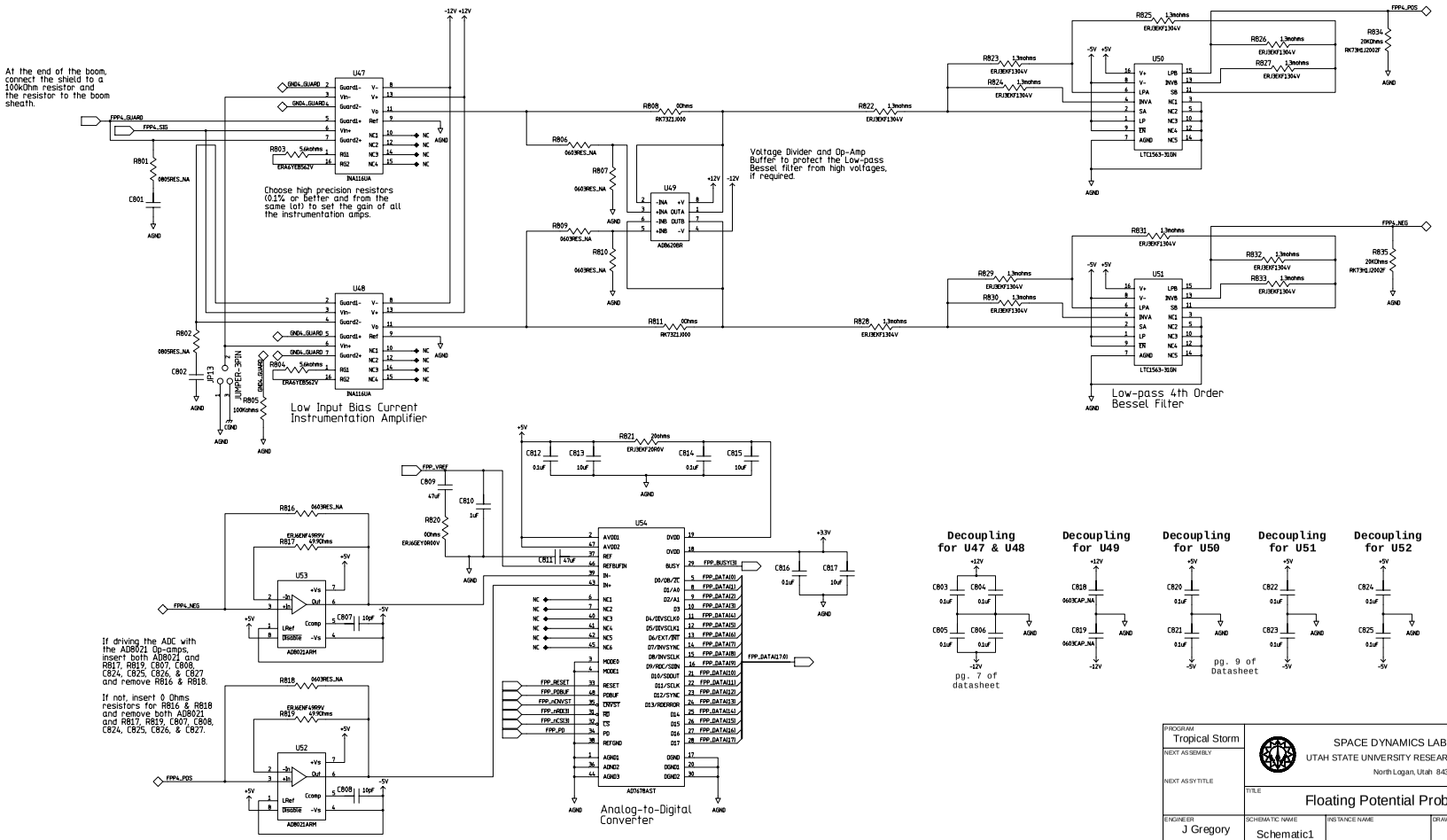

PROGRAM: Tropical Storm	SPACE DYNAMICS LABORATORY, UTAH STATE UNIVERSITY RESEARCH FOUNDATION, North Logan, Utah 84341				
NEXT ASSEMBLY	TITLE: Floating Potential Probe 4 Interface				
NEXT ASSY TITLE					
ENGINEER: J Gregory	SCHEMATIC NAME: Schematic1	INSTANCE NAME:	DRAWING NUMBER: 61-0010	SCH REV: -	
LAST MODIFIED: 6/27/2005	SCHEMATIC: OF	INSTANCE: OF	SCH-INST SHEET: 08 OF 10	TOTAL SCHEMATIC PAGES: 8 OF 10	

Form No. QF0412 Rev D

PLD & Accessories

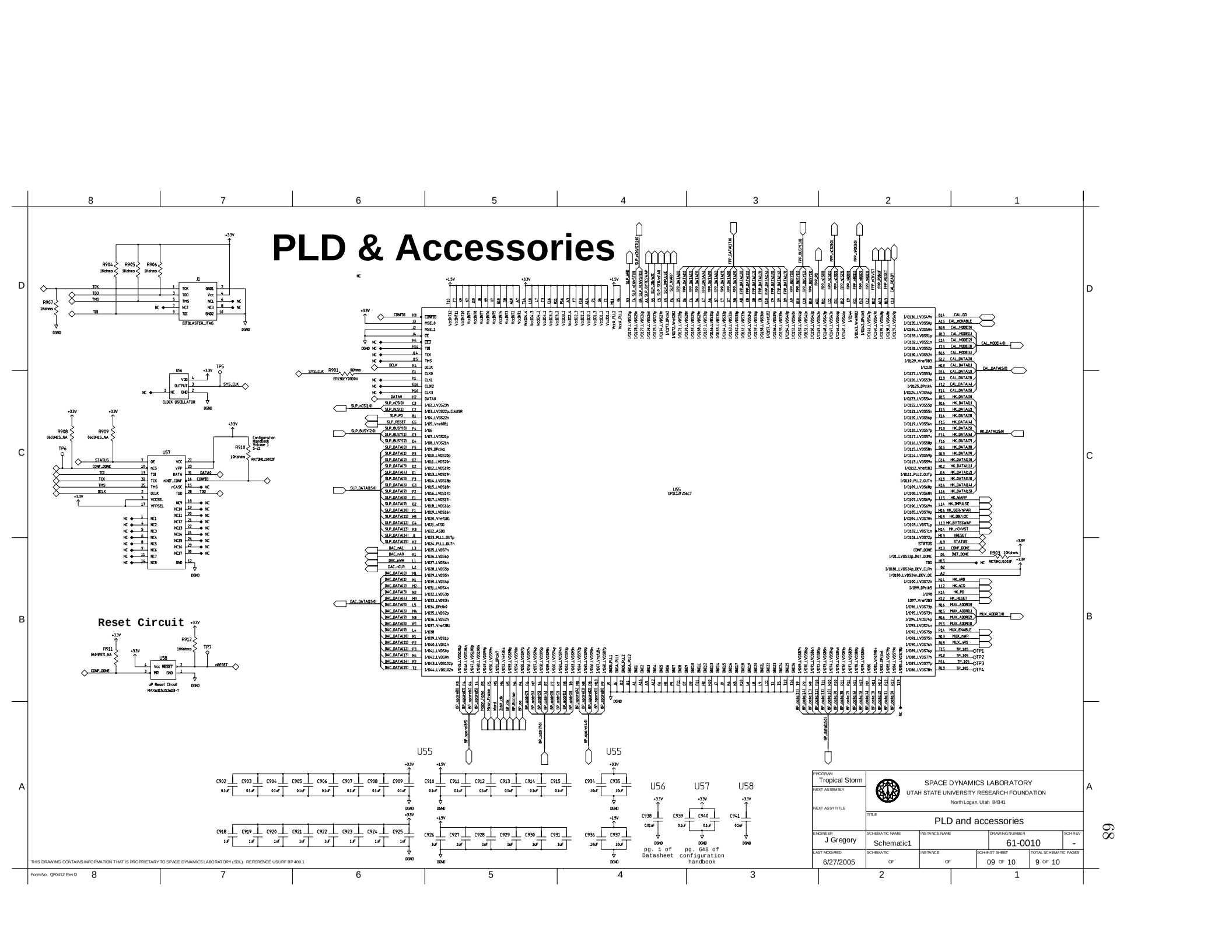

Backplane

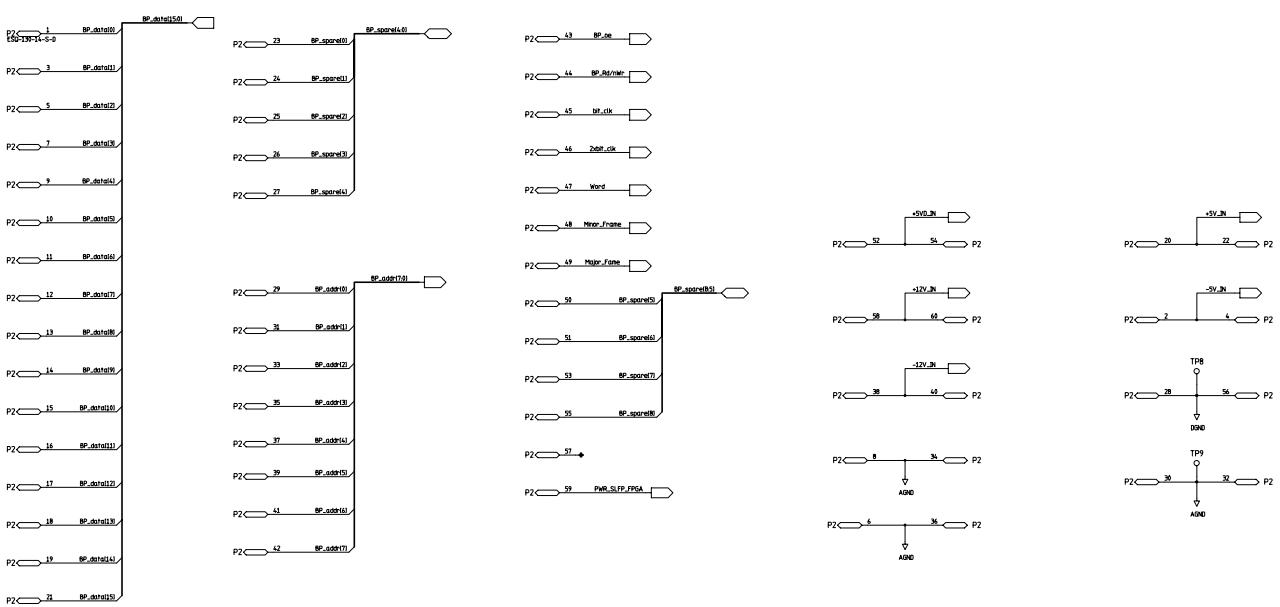

PROGRAM: Tropical Storm	SPACE DYNAMICS LABORATORY UTAH STATE UNIVERSITY RESEARCH FOUNDATION North Logan, Utah 84341				
NEXT ASSEMBLY					
NEXT ASSY TITLE	TITLE: Backplane				
ENGINEER: J Gregory	SCHEMATIC NAME: Schematic1	INSTANCE NAME:	DRAWING NUMBER: 61-0010		SCH REV: -
LAST MODIFIED: 6/27/2005	SCHEMATIC: OF	INSTANCE: OF	SCH-INST SHEET: 10 OF 10	TOTAL SCHEMATIC PAGES: 10 OF 10	

Appendix B

PCB Layout Schematics

The following drawings (fig **??**) show the layout of the PCB for the USU-FPP.

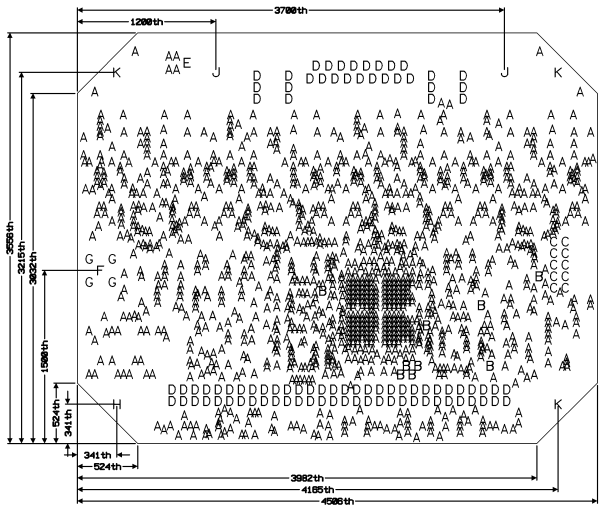

NOTES:

1. FABRICATE PER IPC-6012 CLASS 3.
2. BOARD CONSISTS OF 10 LAYERS OF CIRCUITRY EACH VIEWED FROM THE TOP SIDE. SEE STACKUP FOR OVERALL DIMENSIONS AND INDIVIDUAL LAYER REQUIREMENTS.
3. MATERIAL: ROGERS 4350 WITH Tg OF 250 C MINIMUM.
4. ALL TRACE WIDTHS ARE FINISH DIMENSIONS WITH ±10% TOLERANCE UNLESS OTHERWISE SPECIFIED IN THE STACKUP BELOW.
5. HOLE DIMENSIONS ARE FINISH SIZES WITH ±0.003 INCH TOLERANCE UNLESS OTHERWISE SPECIFIED IN THE DRILL TABLE. VIAs ARE TO BE HELD TO THE SAME SPECIFICATION AS OTHER HOLES.
6. HOLE PLATING TO BE 0.001 INCH NOMINAL +0.002 INCH -0.0002 INCH. SMEAR REMOVAL REQUIRED PER IPC-6012 PARAGRAPH 3.6.2.6.
7. BOARD FINISH: SOLDER MASK OVER BARE COPPER THEN HASL. HOLES SMALLER THAN 0.014 INCH MAY BE PLUGGED. THE SOLDER MASK SHALL BE LIQUID PHOTO-IMAGEABLE IN THE COLOR GREEN.
8. SOLDERMASK CLEARANCES ARE PLOTTED THE SAME SIZE AS THE OUTER PAD, THE VENDOR WILL ADJUST TO MEET THEIR REQUIREMENTS.
9. SILK SCREEN LEGEND USING NON-CONDUCTIVE WHITE EPOXY INK.
10. REMOVE ALL LEGEND INK AND SOLDER MASK FROM PADS UNLESS OTHERWISE SPECIFIED.
11. ADD DATE CODE, MANUFACTURING CODE, AND MANUFACTURES SERIAL NUMBER TO THE BOARD AT THE PLACES INDICATED ON THE LEGEND LAYER.
12. MECHANICAL TOLERANCE UNLESS OTHERWISE NOTED +- 0.005 INCH.
13. ALL VIAS (HOLE DIAMETER 0.010") TO BE SILVER EPOXY FILLED AND SOLDERMASKED

STACKUP	LAYER DESCRIPTION	LAYER NAME	FINISH COPPER WEIGHT	IMPEDANCE OHM
	TOP LEGEND	LEGEND_TOP		
	TOP SOLDER MASK	SM_TOP		
	TOP SIDE TRACE	LAYER1	0.5 OZ	NONE
	INTERNAL TRACE	LAYER2	0.5 OZ	NONE
	-12V,-5V,+3.3V PLANE	LAYER3	0.5 OZ	NONE
	CASE GROUND PLANE	LAYER4	0.5 OZ	NONE
0.063" ±15%	AGND, +1.5VD PLANE	LAYER5	0.5 OZ	NONE
	+5V, +5VD PLANE	LAYER6	0.5 OZ	NONE
	CASE GROUND PLANE	LAYER7	0.5 OZ	NONE
	DGND, +12V PLANE	LAYER8	0.5 OZ	NONE
	INTERNAL TRACE	LAYER9	0.5 OZ	NONE
	BOTTOM SIDE TRACE	LAYER10	0.5 OZ	NONE
	BOTTOM SOLDER MASK	SM_BOT		
	BOTTOM LEGEND	LEGEND_BOT		

Through Holes			
Symbol	Diameter (in)	Plated	Quantity
A	0.0100	Yes	1350
B	0.0350	Yes	9
C	0.0410	Yes	10
D	0.0450	Yes	89
E	0.0590	Yes	1
F	0.0640	Yes	1
G	0.0700	Yes	4
H	0.1130	No	1
J	0.1250	No	2
K	0.1200	No	3

PROGRAM: Tropical Storm	SPACE DYNAMICS LABORATORY			
NEXT ASSEMBLY	UTAH STATE UNIVERSITY RESEARCH FOUNDATION			
NEXT ASSY TITLE	North Logan, Utah 84341			
ENGINEER: J Gregory				
LAST MODIFIED: 6/27/95	LAYER: FAB	TITLE: SLP - FPP	DRAWING NUMBER: 61-0010	PWB REV: -

Form Number QF0419 Rev A

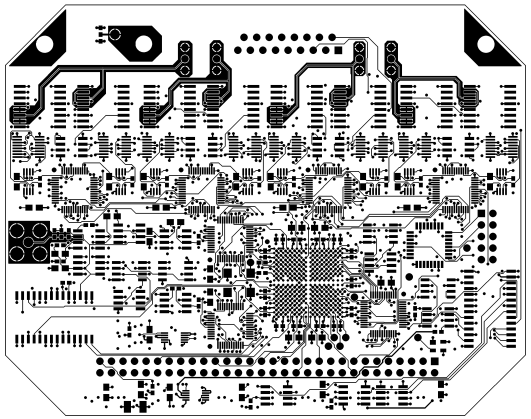

PROGRAM: Tropical Storm	SPACE DYNAMICS LABORATORY			
NEXT ASSEMBLY	UTAH STATE UNIVERSITY RESEARCH FOUNDATION			
NEXT ASSY TITLE	North Logan, Utah 84341			
ENGINEER: J Gregory				
LAST MODIFIED: 6/27/95	LAYER: LAYER 1	TITLE: SLP - FPP	DRAWING NUMBER: 61-0010	PWB REV: -

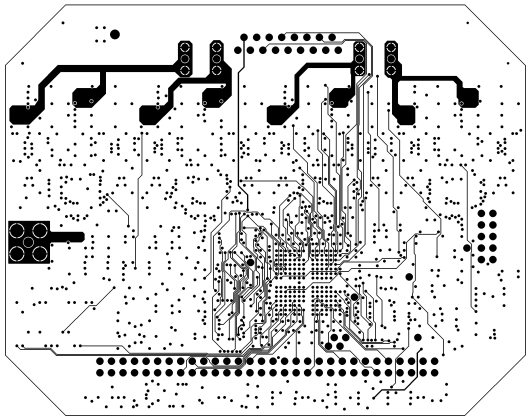

PROGRAM: Tropical Storm	SPACE DYNAMICS LABORATORY			
NEXT ASSEMBLY	UTAH STATE UNIVERSITY RESEARCH FOUNDATION			
NEXT ASSY TITLE	North Logan, Utah 84341			
ENGINEER: J Gregory				
LAST MODIFIED: 6/27/05	LAYER: LAYER 2	TITLE: SLP - FPP	DRAWING NUMBER: 61-0010	PWB REV: -

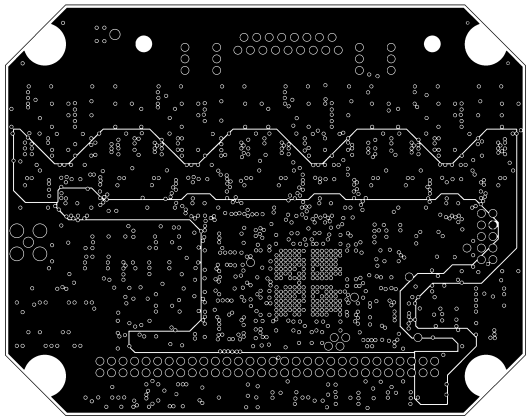

PROGRAM: Tropical Storm	SPACE DYNAMICS LABORATORY			
NEXT ASSEMBLY	UTAH STATE UNIVERSITY RESEARCH FOUNDATION			
NEXT ASSY TITLE	North Logan, Utah 84341			
ENGINEER: J Gregory				
LAST MODIFIED: 6/27/95	LAYER: LAYER 3	TITLE: SLP - FPP	DRAWING NUMBER: 61-0010	PWB REV: -

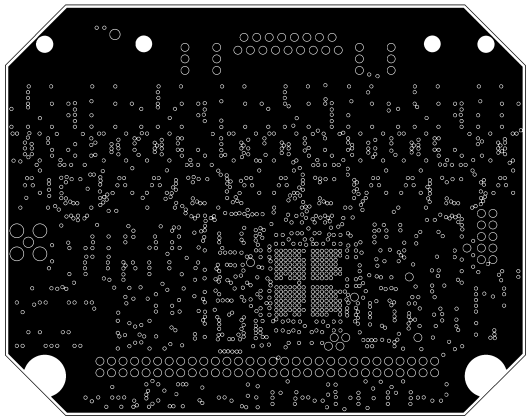

PROGRAM: Tropical Storm	SPACE DYNAMICS LABORATORY			
NEXT ASSEMBLY	UTAH STATE UNIVERSITY RESEARCH FOUNDATION			
NEXT ASSY TITLE	North Logan, Utah 84341			
ENGINEER: J Gregory				
LAST MODIFIED: 6/27/95	LAYER: LAYER 4	TITLE: SLP - FPP	DRAWING NUMBER: 61-0010	PWB REV: -

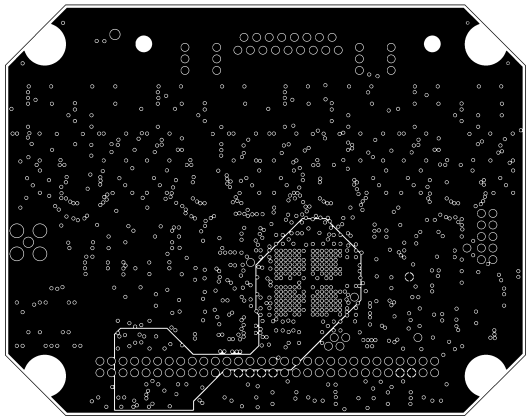

PROGRAM: Tropical Storm	SPACE DYNAMICS LABORATORY			
NEXT ASSEMBLY	UTAH STATE UNIVERSITY RESEARCH FOUNDATION			
NEXT ASSY TITLE	North Logan, Utah 84341			
ENGINEER: J Gregory				
LAST MODIFIED: 6/27/95	LAYER: LAYER 5	TITLE: SLP - FPP	DRAWING NUMBER: 61-0910	PWB REV: -

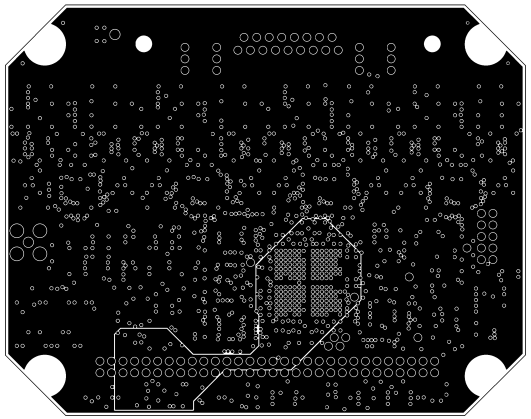

PROGRAM: Tropical Storm	SPACE DYNAMICS LABORATORY			
NEXT ASSEMBLY	UTAH STATE UNIVERSITY RESEARCH FOUNDATION			
NEXT ASSY TITLE	North Logan, Utah 84341			
ENGINEER: J Gregory				
LAST MODIFIED: 6/27/95	LAYER: LAYER 6	TITLE: SLP - FPP	DRAWING NUMBER: 61-0010	PWB REV: -

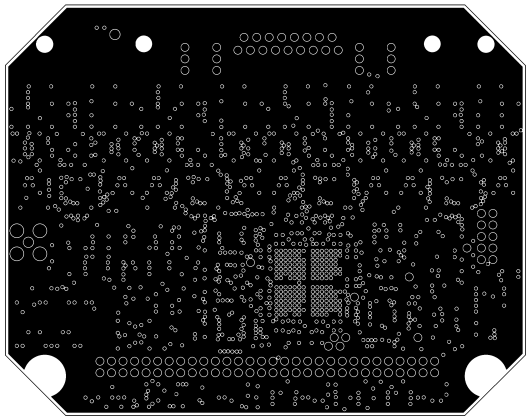

PROGRAM: Tropical Storm	SPACE DYNAMICS LABORATORY			
NEXT ASSEMBLY	UTAH STATE UNIVERSITY RESEARCH FOUNDATION			
NEXT ASSY TITLE	North Logan, Utah 84341			
ENGINEER: J Gregory				
LAST MODIFIED: 6/27/95	LAYER: LAYER 7	TITLE: SLP - FPP	DRAWING NUMBER: 61-0910	PWB REV: -

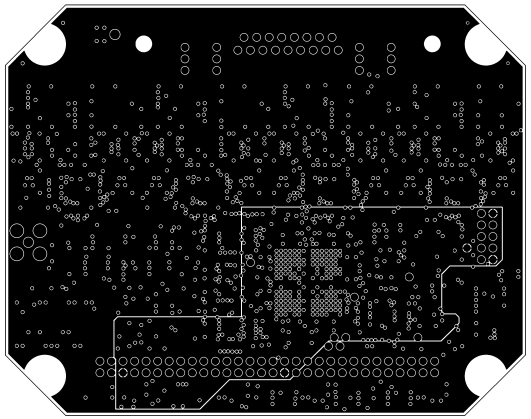

PROGRAM: Tropical Storm	SPACE DYNAMICS LABORATORY			
NEXT ASSEMBLY	UTAH STATE UNIVERSITY RESEARCH FOUNDATION			
NEXT ASSY TITLE	North Logan, Utah 84341			
ENGINEER: J Gregory				
LAST MODIFIED: 6/27/95	LAYER: LAYER 8	TITLE: SLP - FPP	DRAWING NUMBER: 61-0910	PWB REV: -

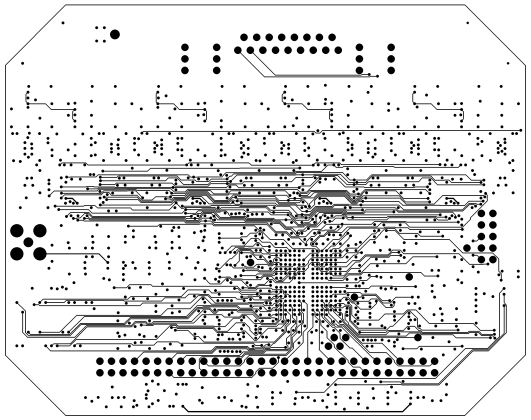

PROGRAM: Tropical Storm	SPACE DYNAMICS LABORATORY			
NEXT ASSEMBLY	UTAH STATE UNIVERSITY RESEARCH FOUNDATION			
NEXT ASSY TITLE	North Logan, Utah 84341			
ENGINEER: J Gregory				
LAST MODIFIED: 6/27/05	LAYER: LAYER 9	TITLE: SLP - FPP	DRAWING NUMBER: 61-0010	PWB REV: -

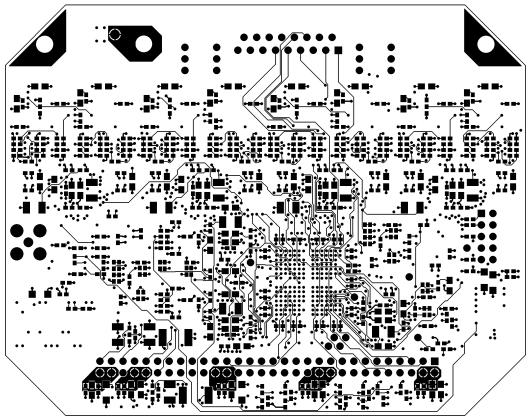

PROGRAM: Tropical Storm	SPACE DYNAMICS LABORATORY			
NEXT ASSEMBLY	UTAH STATE UNIVERSITY RESEARCH FOUNDATION			
NEXT ASSY TITLE	North Logan, Utah 84341			
ENGINEER: J Gregory				
LAST MODIFIED: 6/27/95	LAYER: LAYER 10	TITLE: SLP - FPP	DRAWING NUMBER: 61-0010	PWB REV: -

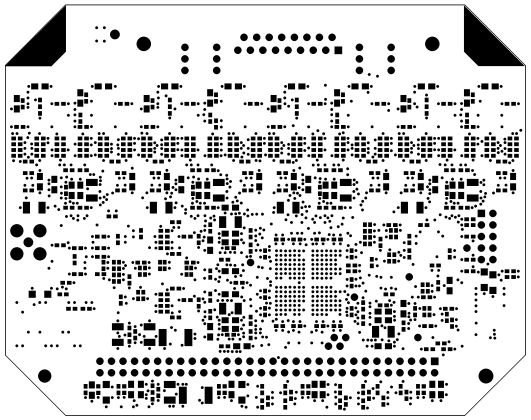

PROGRAM: Tropical Storm	SPACE DYNAMICS LABORATORY			
NEXT ASSEMBLY	UTAH STATE UNIVERSITY RESEARCH FOUNDATION			
NEXT ASSY TITLE	North Logan, Utah 84341			
ENGINEER: J Gregory				
LAST MODIFIED: 6/27/95	LAYER: SM_BOT	TITLE: SLP - FPP	DRAWING NUMBER: 61-0010	PWB REV: -

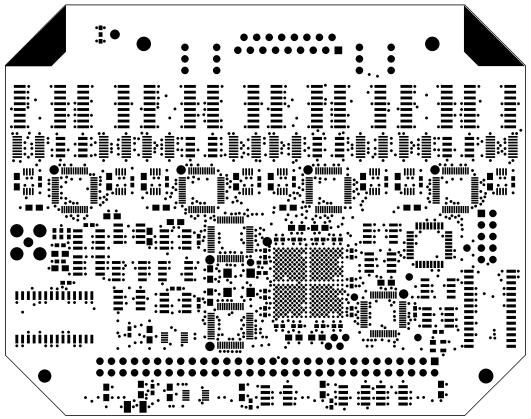

PROGRAM: Tropical Storm	SPACE DYNAMICS LABORATORY			
NEXT ASSEMBLY	UTAH STATE UNIVERSITY RESEARCH FOUNDATION			
NEXT ASSY TITLE	North Logan, Utah 84341			
ENGINEER: J Gregory				
LAST MODIFIED: 6/27/95	LAYER: SM_TOP	TITLE: SLP - FPP	DRAWING NUMBER: 61-0010	PWB REV: -

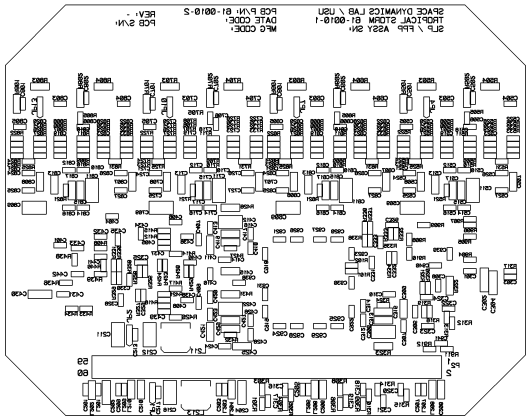

PROGRAM: Tropical Storm	SPACE DYNAMICS LABORATORY			
NEXT ASSEMBLY	UTAH STATE UNIVERSITY RESEARCH FOUNDATION			
NEXT ASSY TITLE	North Logan, Utah 84341			
ENGINEER: J Gregory				
LAST MODIFIED: 6/27/95	LAYER: LEGEND_BOT	TITLE: SLP - FPP	DRAWING NUMBER: 61-0010	PWB REV: -

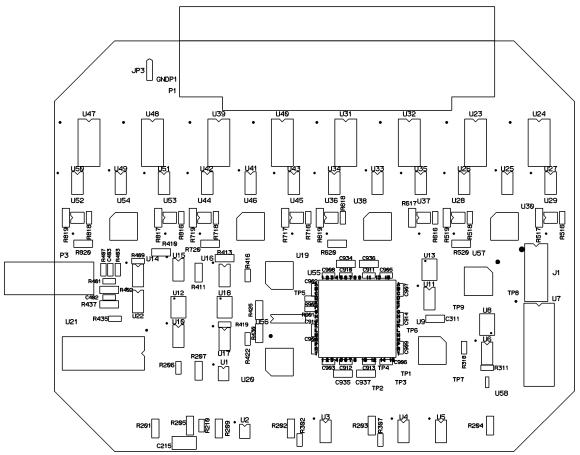

PROGRAM: Tropical Storm	SPACE DYNAMICS LABORATORY			
NEXT ASSEMBLY	UTAH STATE UNIVERSITY RESEARCH FOUNDATION			
NEXT ASSY TITLE	North Logan, Utah 84341			
ENGINEER: J Gregory				
LAST MODIFIED: 6/27/95	LAYER: LEGEND_TOP	TITLE: SLP - FPP	DRAWING NUMBER: 61-0910	PWB REV: -

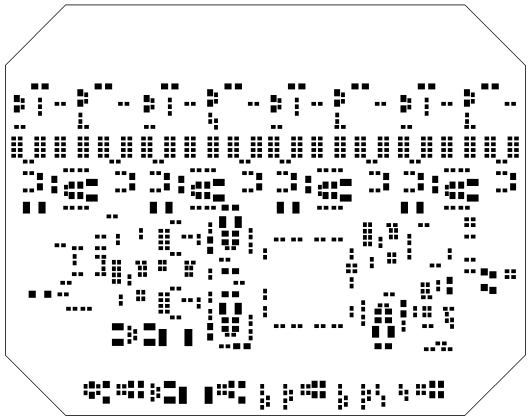

PROGRAM: Tropical Storm	SPACE DYNAMICS LABORATORY			
NEXT ASSEMBLY	UTAH STATE UNIVERSITY RESEARCH FOUNDATION			
NEXT ASSY TITLE	North Logan, Utah 84341			
ENGINEER: J Gregory				
LAST MODIFIED: 6/27/05	LAYER: SP_BOT	TITLE: SLP - FPP	DRAWING NUMBER: 61-0010	PWB REV: -

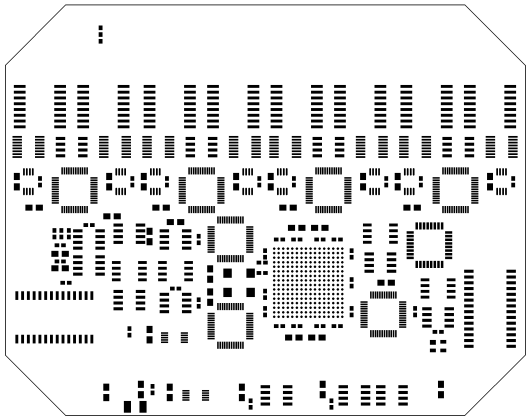

PROGRAM: Tropical Storm	SPACE DYNAMICS LABORATORY			
NEXT ASSEMBLY	UTAH STATE UNIVERSITY RESEARCH FOUNDATION			
NEXT ASSY TITLE	North Logan, Utah 84341			
ENGINEER: J Gregory				
LAST MODIFIED: 6/27/95	LAYER: SP_TOP	TITLE: SLP - FPP	DRAWING NUMBER: 61-0010	PWB REV: -

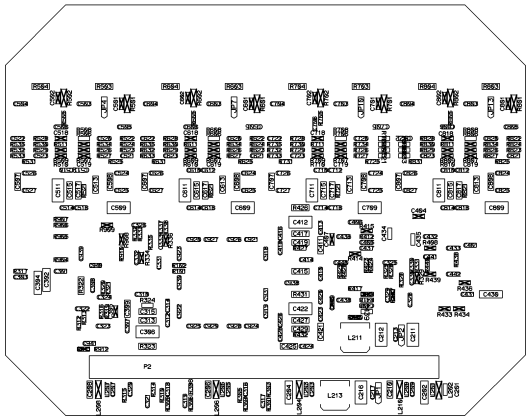

PROGRAM: Tropical Storm	SPACE DYNAMICS LABORATORY			
NEXT ASSEMBLY	UTAH STATE UNIVERSITY RESEARCH FOUNDATION			
NEXT ASSY TITLE	North Logan, Utah 84341			
ENGINEER: J Gregory				
LAST MODIFIED: 6/27/95	LAYER: ASSY_BOT	TITLE: SLP - FPP	DRAWING NUMBER: 61-0910	PWB REV: -

ASSEMBLY NOTES:
1. ASSEMBLE PER ANSI/IPC-A-610 Acceptability of Electronic Assemblies CLASS 3.
2. ASSEMBLE PER ANSI/J-STD-001 Requirements for Soldered Electrical and Electronic Assemblies.

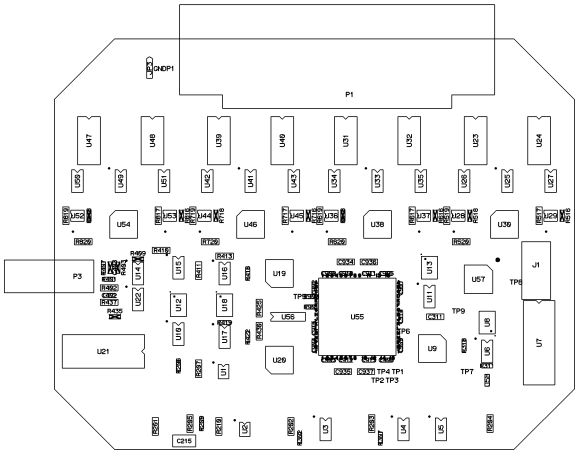

PROGRAM: Tropical Storm	SPACE DYNAMICS LABORATORY UTAH STATE UNIVERSITY RESEARCH FOUNDATION North Logan, Utah 84341				
NEXT ASSEMBLY					
NEXT ASSY TITLE					
ENGINEER: J Gregory					
LAST MODIFIED: 6/27/95	LAYER: ASSY_TOP	TITLE: SLP - FPP	DRAWING NUMBER: 61-0010	PWB REV: -	

Form Number QF0419 Rev A